Available online at www.sciencedirect.com

ScienceDirect

Geochimica et Cosmochimica Acta 221 (2018) 296–317

Geochimica et Cosmochimica Acta

www.elsevier.com/locate/gca

A multielement isotopic study of refractory FUN and F CAIs: Mass-dependent and mass-independent isotope effects

Levke Kööp [a,b,c,*], Daisuke Nakashima [d,e], Philipp R. Heck [a,b,c], Noriko T. Kita [d], Travis J. Tenner [d,f], Alexander N. Krot [g], Kazuhide Nagashima [g], Changkun Park [g,h], Andrew M. Davis [a,b,c,i]

[a] Department of the Geophysical Sciences, The University of Chicago, Chicago, IL 60637, USA
[b] Chicago Center for Cosmochemistry, The University of Chicago, Chicago, IL 60637, USA
[c] Robert A. Pritzker Center for Meteoritics and Polar Studies, Field Museum of Natural History, Chicago, IL, USA
[d] Department of Geoscience, University of Wisconsin, Madison, WI 53706, USA
[e] Division of Earth and Planetary Material Sciences, Faculty of Science, Tohoku University, Aoba, Sendai, Miyagi 980-8578, Japan
[f] Chemistry Division, Nuclear and Radiochemistry, Los Alamos National Laboratory, MSJ514, Los Alamos, NM 87545, USA
[g] Hawai'i Institute of Geophysics and Planetology, School of Ocean and Earth Science and Technology, University of Hawai'i at Mānoa, Honolulu, HI, USA
[h] Korea Polar Research Institute, Incheon 21990, Republic of Korea
[i] Enrico Fermi Institute, The University of Chicago, Chicago, IL 60637, USA

Received 14 October 2016; accepted in revised form 19 April 2017; available online 26 April 2017

Abstract

Calcium-aluminum-rich inclusions (CAIs) are the oldest dated objects that formed inside the Solar System. Among these are rare, enigmatic objects with large mass-dependent fractionation effects (F CAIs), which sometimes also have large nucleosynthetic anomalies and a low initial abundance of the short-lived radionuclide ^{26}Al (FUN CAIs). We have studied seven refractory hibonite-rich CAIs and one grossite-rich CAI from the Murchison (CM2) meteorite for their oxygen, calcium, and titanium isotopic compositions. The ^{26}Al-^{26}Mg system was also studied in seven of these CAIs. We found mass-dependent heavy isotope enrichment in all measured elements, but never simultaneously in the same CAI. The data are hard to reconcile with a single-stage melt evaporation origin and may require reintroduction or reequilibration for magnesium, oxygen and titanium after evaporation for some of the studied CAIs.

The initial ^{26}Al/^{27}Al ratios inferred from model isochrons span a range from $<1 \times 10^{-6}$ to canonical ($\sim 5 \times 10^{-5}$). The CAIs show a mutual exclusivity relationship between inferred incorporation of live ^{26}Al and the presence of resolvable anomalies in ^{48}Ca and ^{50}Ti. Furthermore, a relationship exists between ^{26}Al incorporation and Δ^{17}O in the hibonite-rich CAIs (i.e., ^{26}Al-free CAIs have resolved variations in Δ^{17}O, while CAIs with resolved ^{26}Mg excesses have Δ^{17}O values close to −23‰). Only the grossite-rich CAI has a relatively enhanced Δ^{17}O value (∼−17‰) in spite of a near-canonical ^{26}Al/^{27}Al. We interpret these data as indicating that fractionated hibonite-rich CAIs formed over an extended time period and sampled multiple stages in the isotopic evolution of the solar nebula, including: (1) an ^{26}Al-poor nebula with large positive and negative anomalies in ^{48}Ca and ^{50}Ti and variable Δ^{17}O; (2) a stage of ^{26}Al-admixture, during which anomalies in ^{48}Ca and ^{50}Ti had

* Corresponding author at: Department of the Geophysical Sciences, The University of Chicago, Chicago, IL 60637, USA.
E-mail address: koeoep@uchicago.edu (L. Kööp).

http://dx.doi.org/10.1016/j.gca.2017.04.029

been largely diluted and a $\Delta^{17}O$ value of $\sim -23‰$ had been achieved in the CAI formation region; and (3) a nebula with an approximately canonical level of ^{26}Al and a $\Delta^{17}O$ value of $\sim -23‰$ in the CAI formation region.

Keywords: Fractionated and unidentified nuclear (FUN); CAI; Hibonite; Meteorites; Solar nebula; Oxygen isotopes; Aluminum-26; Magnesium isotopes; Titanium isotopes; Calcium isotopes; Mass-dependent fractionation

1. INTRODUCTION

The enigmatic isotopic characteristics of FUN (fractionated and unidentified nuclear effects) CAIs (calcium-, aluminum-rich inclusions) are believed to hold important clues to the nucleosynthetic inventory of the Solar System as well as its evolution. In comparison to most CAIs from CV chondrites (hereafter referred to as regular CAIs), which formed with a high abundance of the short-lived radionuclide (SLR) ^{26}Al (i.e., the canonical initial $^{26}Al/^{27}Al$ ratio ($(^{26}Al/^{27}Al)_0$) of $\sim 5.2 \times 10^{-5}$; Jacobsen et al., 2008), many FUN CAIs lack resolvable radiogenic excesses of the daughter nuclide ^{26}Mg (Krot et al., 2014b, and references therein; Park et al., 2017; Williams et al., 2017) or have a lower inferred $(^{26}Al/^{27}Al)_0$ than the canonical value (e.g., $\sim 5.2 \times 10^{-8}$ for HAL, $(2.2 \pm 1.1) \times 10^{-6}$ for C1; Park et al., 2017). This ^{26}Al-poor characteristic of FUN CAIs is coupled with large mass-independent anomalies of nucleosynthetic origin that are one or two orders of magnitude greater than those in regular CAIs (e.g., up to ~46‰ enrichments or depletions in neutron-rich isotopes like ^{48}Ca, ^{50}Ti, ^{54}Cr, ^{58}Fe, and up to 4‰ effects in strontium, barium, neodymium and samarium isotopes; Birck, 2004; Liu et al., 2009; Dauphas and Schauble, 2016; and references therein). As such large nucleosynthetic anomalies are hard to reconcile with late formation after most ^{26}Al had decayed, FUN CAIs are often considered to have formed prior to arrival of fresh ^{26}Al in the solar nebula (e.g., 'late injection scenario', Fahey et al., 1987; Wood, 1998; Sahijpal and Goswami, 1998). A recent ^{182}Hf-^{182}W study of an ^{26}Al-poor ($(^{26}Al/^{27}Al)_0$ of $\sim 3 \times 10^{-6}$)) FUN CAI supports this interpretation, as the uncertainty of the inferred age would allow for formation earlier than regular CAIs, but not for formation as late as required if the low $^{26}Al/^{27}Al$ was attributed to its decay (Holst et al., 2013).

FUN CAIs differ from regular CAIs not only in their mass-independent isotope effects, but also in the large degrees of mass-dependent heavy isotope enrichments observed in elements like oxygen, magnesium, silicon, calcium, and titanium (e.g., Krot et al., 2014b, and references therein; Park et al., 2017; Williams et al., 2017). These observations seemed to suggest a link between the availability of anomalous nucleosynthetic components and conditions favorable for creating large mass-dependent fractionation effects; the latter is commonly attributed to high degrees of melt evaporation of low-temperature precursors. However, recent efforts to identify and study more CAIs with FUN properties (e.g., Wimpenny et al., 2014; Park et al., 2014, 2017) show that the F and UN characteristics can be decoupled, i.e., F CAIs are highly fractionated, lack large nucleosynthetic anomalies and have approximately canonical $(^{26}Al/^{27}Al)_0$. In addition, there are UN CAIs, which lack mass-dependent effects, but have larger anomalies than regular CV CAIs and low $(^{26}Al/^{27}Al)_0$, e.g., platy hibonite crystals (PLACs) and PLAC-like CAIs (Zinner et al., 1986; Ireland, 1988, 1990; Liu et al., 2009; Kööp et al., 2016a).

While the isotopic record preserved in FUN and F CAIs (collectively referred to here as F(UN) CAIs) may yield important clues for our understanding of the stellar sources that contributed material to the Solar System and the physicochemical conditions that characterized the solar nebula, much of this record remains poorly understood. For example, while a late arrival of ^{26}Al to the protoplanetary disk is favored to explain the low $(^{26}Al/^{27}Al)_0$ in FUN and UN CAIs, its origin remains unclear (i.e., large-scale heterogeneity in the protosolar molecular cloud or direct injection from an unidentified stellar source). Similarly, it is not yet clear what the relative roles of age, mixing, and thermal processing are for the interpretation of nucleosynthetic anomalies of different magnitudes. In addition, inconsistencies exist between mass-dependent fractionation effects in different elements (e.g., uncorrelated effects in calcium and titanium) for F(UN) and for regular CAIs (e.g., Ireland et al., 1992; Kööp et al., 2016b) when compared with experimental studies and volatility considerations.

To improve our understanding of these issues, we conducted a multielement isotopic study of seven newly identified hibonite-rich CAIs and one grossite-rich CAI with mass-dependent fractionation effects. The multielement approach allows a better evaluation as to which reservoirs were sampled by these highly refractory mass-fractionated CAIs and what the relationship between ^{26}Al, nucleosynthetic anomalies and oxygen isotopes was. In addition, it allows for a systematic investigation of the relationship between mass-dependent signatures in different elements.

2. METHODS

2.1. Sample recovery, selection and preparation

The hibonite-rich inclusions were separated from the Murchison CM2 chondrite. They were characterized and prepared with PLAC-like CAIs (Kööp et al., 2016a) and SHIBs (i.e., spinel-hibonite inclusions; Kööp et al., 2016b). The CAIs presented here are distinct from those presented in our PLAC and SHIB studies, based on their mass-dependent isotope effects and often also other properties such as chemical composition, mineralogy and morphology. Some of the samples (CAIs 1–9–1, 2–5–1, 2–6–1, 2–6–6) were recovered from the dense fraction of a freshly

disaggregated Murchison rock fragment (not acid-treated, approximately 92 g from Field Museum specimen ME 2644). Others (i.e., CAIs 1–10–3, 2–2–1, 2–8–3) were picked from an existing Murchison HF-HCl acid residue (Amari et al., 1994). For brevity, we refer to the samples as CAIs below, but acknowledge that they may in fact be fragments of larger CAIs that could have been liberated by parent body processes or sample preparation.

As described in Kööp et al. (2016a,b), the CAIs were cleaned, mounted close to the centers of one-inch epoxy rounds alongside standard grains, polished and coated with carbon. After ion probe analysis, some of the mounts were polished and recoated in gold and/or carbon.

2.2. Electron microscopy

The CAIs were characterized with a Zeiss EVO 60 SEM at the Field Museum of Natural History, and a JEOL JSM-5800LV SEM and a TESCAN LYRA3 SEM/FIB at the University of Chicago, all equipped with Oxford Instruments energy dispersive spectroscopy (EDS) systems. The samples were analyzed by EDS and imaged using backscattered electrons (BSE) and secondary electrons both prior to and after polishing. The images and compositional information were then used for identifying the most suitable locations for isotope analysis.

Elemental X-ray maps were produced with the TESCAN LYRA3 SEM/FIB. As analyses collected in areas containing epoxy or residual gold coating can be biased, the map data were processed after collection by removing point analyses associated with high carbon or gold signals.

2.3. Quantitative chemical analysis

Most quantitative chemical analyses of hibonite grains were performed with a Cameca SX-50 electron probe microanalyzer (EPMA) at the University of Chicago. The conditions were identical to those described by Kööp et al. (2016a,b). Additional quantitative data were collected using an Oxford Instruments Wave 500 wavelength-dispersive spectrometer (WDS) on the TESCAN LYRA3 SEM/FIB. For this, we used the same standard minerals, a beam current of ~10 nA, and an acceleration voltage of 15 kV.

2.4. Isotopic analyses

2.4.1. Oxygen

The CAIs were measured for their oxygen isotopic compositions with the WiscSIMS Cameca ims-1280 (Kita et al., 2009, 2010) with conditions identical to those described by Kööp et al. (2016a,b). Oxygen isotopes were detected in multicollection mode using a Faraday cup (FC) for $^{16}O^-$ and electron multipliers (EM) for $^{17}O^-$ and $^{18}O^-$. Two to four spots were analyzed in every CAI. A San Carlos olivine standard was analyzed and used for bracketing of unknown analyses (running standard) and appropriate WiscSIMS mineral standards were used to correct for the instrumental bias affecting the different analyzed phases (here: Madagascar hibonite, Al-Mg spinel, corundum). As no grossite standard was available, Madagascar hibonite was used to correct grossite analysis. The SIMS pits were checked with the SEM, which did not reveal any problems (i.e., only primary minerals were sampled; SIMS pits did not overlap with cracks or grain boundaries). For all samples, oxygen was the first element measured for its isotopic composition.

2.4.2. Aluminum-magnesium

Magnesium isotopes in hibonite grains were analyzed using a monocollection EM detector combined with an additional FC detector for simultaneous detection of ^{27}Al with ^{25}Mg (Kita et al., 2012; Ushikubo et al., 2013) using a ~9 μm diameter primary O^- beam. Many conditions (i.e., counting times, number of cycles) were identical to those described by Kööp et al. (2016a). Specific differences to the aforementioned protocol were that the primary beam current had to be increased for some hibonite grains due to low MgO contents. Grains with MgO contents< 1 wt% were measured with a ~0.5 nA primary beam. For more MgO-rich hibonites, a ~0.15 nA beam was used. The resulting secondary $^{24}Mg^+$ signals were within a range of $(0.4–1.6) \times 10^5$ cps. A WiscSIMS Madagascar hibonite (MH) standard was analyzed to determine the relative sensitivity factor (RSF) between $^{27}Al^+$ and $^{24}Mg^+$ signals, which is used to correct the measured $^{27}Al/^{24}Mg$ ratios of unknowns, as was done in previous studies (Ireland, 1988; Liu et al., 2012; Kööp et al., 2016a,b). The chemical difference between the Madagascar hibonite standard and meteoritic hibonites may have introduced a small bias in the corrected $^{27}Al/^{24}Mg$ values and inferred $^{26}Al/^{27}Al$ ratios (for a discussion, see Kööp et al., 2016b).

The hibonite analyses were bracketed by measurements of anorthite glass standards with MgO contents comparable to unknowns (1% for MgO-rich and 0.1% for MgO-poor hibonites, respectively; Kita et al., 2012). These were used to estimate the instrumental bias for radiogenic excess ^{26}Mg ($\delta^{26}Mg^*$) and to correct for instrumental mass fractionation in $\delta^{25}Mg$ (the standard has a $\delta^{25}Mg$ of −1.77‰; Kita et al., 2012). A systematic bias introduced by the matrix effect between anorthite and hibonite would not affect $\delta^{26}Mg^*$ outside of quoted uncertainties, but could affect $\delta^{25}Mg$ values. However, based on a comparison of anorthite and Madagascar hibonite standard measurements, this effect is small (not resolved if Madagascar hibonite has a $\delta^{25}Mg = 0‰$).

A single analysis was collected in the grossite-rich CAI 2–6–1. Grossite was analyzed with a ~0.15 nA beam (alongside and under identical conditions as the more MgO-rich hibonite grains described above). Due to the low MgO abundance in grossite, the secondary signals were low (~1, ~0.1 and ~437 cps for $^{24}Mg^+$, $^{25}Mg^+$ and $^{26}Mg^+$, respectively). Isotope ratios were calculated from the sum of signals collected in 19 cycles to minimize the ratio bias effect (Ogliore et al., 2011). No grossite standard was available, so Madagascar hibonite was used to estimate the RSF and correct the measured $^{27}Al/^{24}Mg$ ratio. This was similar to Makide et al. (2009) and the matrix effect may have resulted in a small bias in $^{27}Al/^{24}Mg$ and $^{26}Al/^{27}Al$ ratios.

Two analyses were collected in a spinel grain in CAI 1–9–1 under identical conditions as those reported by Kööp et al. (2016b).

For analyses of hibonite and spinel, excess ^{26}Mg was calculated using the equation $\delta^{26}Mg^{*} = \delta^{26}Mg - [(1 + \delta^{25}Mg/1000)^{1/\beta} - 1] \times 1000$ (e.g., Davis et al., 2015). The updated β value of 0.5128 was used (Davis et al., 2015). However, no difference outside of quoted uncertainties is observed when the previously recommended β value of 0.514 (Davis et al., 2005) is applied instead. For one-spot analyses, initial $^{26}Al/^{27}Al$ ratios were inferred from model isochrons that assume a normal initial magnesium isotopic composition (i.e., $\delta^{26}Mg^{*}_{0} = 0$).

2.4.3. Calcium and titanium

The conditions for calcium and titanium analyses on the University of Hawai'i Cameca ims-1280 have been reported in detail by Kööp et al. (2016a,b) for hibonite-rich CAIs that were analyzed in the same session as the CAIs presented here. All data presented here were corrected for instrumental mass-fractionation by bracketing unknown analyses with measurements on a Madagascar hibonite standard. The calcium and titanium isotopic compositions of the latter are assumed to correspond to the values listed in Niederer and Papanastassiou (1984) and Niederer et al. (1981), respectively. Any remaining mass-dependent fractionation is interpreted to reflect intrinsic fractionation (F_{Ca} and F_{Ti}) and corrected for using a Rayleigh law, assuming that calcium evaporated as Ca atoms and titanium as TiO_2 molecules, based on evaporation experiments of Zhang et al. (2014). For calcium, $^{44}Ca/^{40}Ca$ was used for normalization, for titanium, data are reported in both the $^{49}Ti/^{47}Ti$ and $^{46}Ti/^{48}Ti$ normalizations. Intrinsic fractionation (F_{Ti} and F_{Ca}) was calculated as $F_{Ti} = -[\Delta^{46}Ti/\{mass(^{48}Ti) - mass(^{46}Ti)\}]$, with $\Delta^{46}Ti = [(^{46}Ti/^{48}Ti)_{measured}/(^{46}Ti/^{48}Ti)_{standard} - 1] \times 1000$ (analogous for $^{49}Ti/^{47}Ti$ normalization and F_{Ca}). Both F_{Ti} and F_{Ca} are given in units of ‰/amu, and positive values indicate heavy isotope enrichment.

3. RESULTS

3.1. Petrologic characteristics

3.1.1. Morphology and mineralogy

Five of the CAIs (2–2–1, 2–5–1, 2–6–6, 2–8–3, and 2–8–7) are single hibonite crystals with inclusions of other minerals. The others are a hibonite aggregate with inclusions of corundum (1–10–3), a platy object consisting of hibonite and spinel (1–9–1), and a grossite-rich object (2–6–1).

CAIs 2–2–1 and 2–8–3 are platy hibonite crystals recovered from the acid residue (Fig. 1). Prior to polishing, the surfaces of both crystals showed abundant hexagonal pits (illustrated for 2–8–3 in Fig. 1a). The polished surfaces of both CAIs reveal round to elongated inclusions of perovskite and voids in the centers (Fig. 1b and c). The elongated voids and perovskite inclusions are oriented in two directions that define ~60 degree angles in both crystals.

CAIs 2–5–1, 2–6–6 and 2–8–7 are stubby hibonite crystals. All three have eroded margins, but for 2–6–6 and 2–5–1, some crystal faces define ~120 degree angles, consistent with their hexagonal crystal system (Fig. 2a and c). CAIs 2–5–1 and 2–6–6 were picked from the non-acid-treated Murchison separate, while 2–8–7 was recovered from the acid-residue. Prior to polishing, the surface of 2–5–1 was found to be covered in fine-grained silicate material (Fig. 2b), which is not apparent in the polished mount (Fig. 2a). All three crystals contain abundant sub-μm-sized refractory metal nuggets (RMN).

CAI 1–9–1 is a hibonite plate partially covered by spinel. Prior to polishing, the spinel had a mottled, grainy texture; the surface of the hibonite is smoother but is embayed (Fig. 3a). Fine-grained silicates partially cover the spinel (Fig. 3a) as well as the edge of the CAI (Fig. 3b).

CAI 1–10–3 is an irregularly shaped aggregate of hibonite crystals recovered from the acid-residue (Fig. 4). Most hibonite crystals contain μm- to sub-μm-sized inclusions of corundum. A single RMN was identified at a corundum-hibonite grain boundary (Fig. 4c).

CAI 2–6–1 is a ~120-μm-sized fragment composed mostly of grossite, and is surrounded by a discontinuous

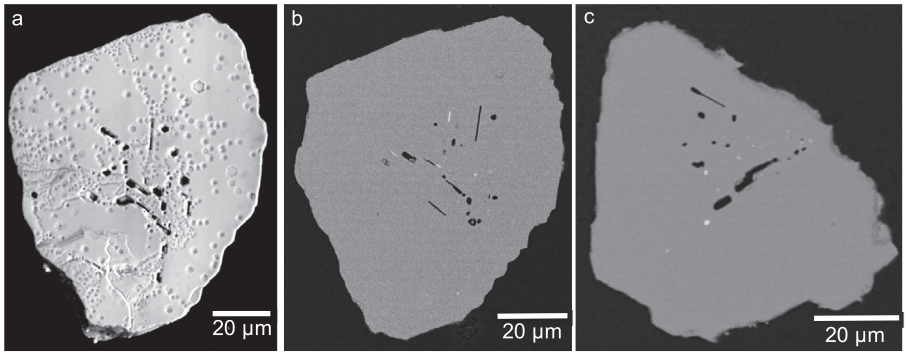

Fig. 1. Platy hibonite grains 2–2–1 and 2–8–3 in BSE. (a) The unpolished surface of platy hibonite 2–8–3 is covered with hexagonal pits and elongated voids. (b) The polished surface of 2–8–3 reveals round to elongated perovskite inclusions and holes, oriented in two different directions. (c) The polished surface of 2–2–1 shows similar elongated and round holes.

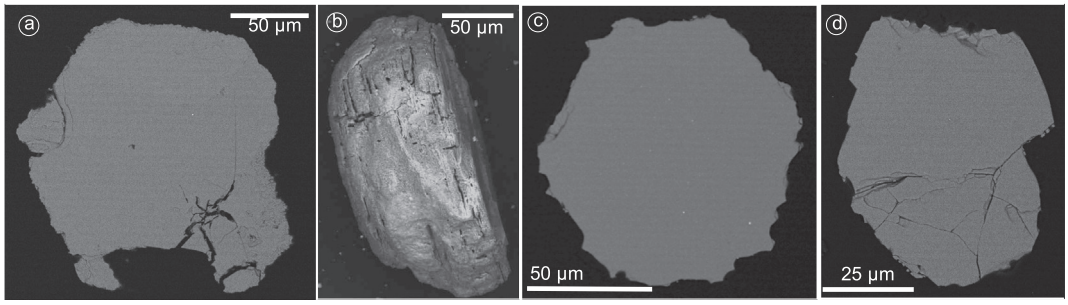

Fig. 2. BSE images of mass-fractionated stubby hibonites 2–5–1, 2–6–6, and 2–8–7. (a) The polished surface of CAI 2–5–1. Some crystal faces define 120 degree angles. (b) The side of grain 2–5–1 before polishing. The grain is covered by fine-grained FeO-rich silicates. (c) Similar to 2–5–1, the faces of 2–6–6 define 120 degree. (d) Grain 2–8–7 has an irregular shape.

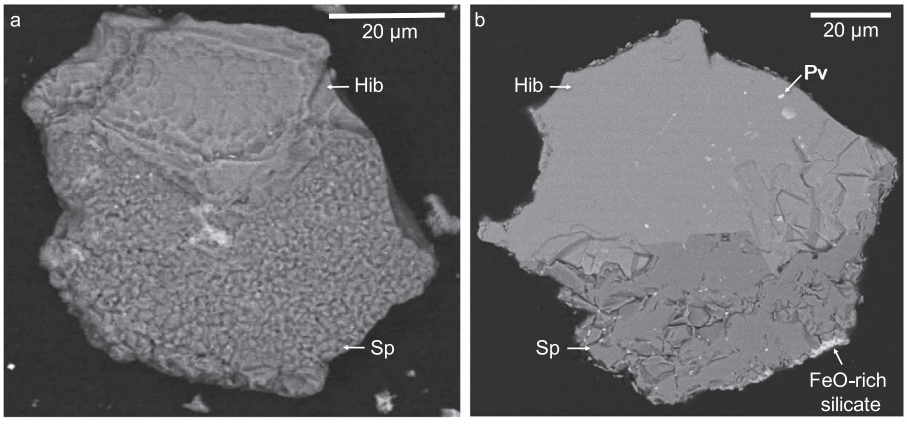

Fig. 3. BSE images of mass-fractionated spinel-hibonite platelet 1–9–1. (a) Before polishing, the hibonite surface shows layers of hibonite with rounded dents, the spinel has a mottled appearance. (b) After polishing, perovskite inclusions are apparent in the hibonite. Abbreviations: Hib – hibonite, Sp – spinel, Pv – perovskite.

rim of FeO-rich silicates (Fig. 5). Set inside the grossite are multiple inclusions, e.g., rounded perovskite grains (≤15 µm) as well as polymineralic assemblages. Assemblages of type 1 (enlarged in Fig. 5c, e and ~5 to 30 µm in diameter) consist of a hibonite core surrounded by a band of amoeboid sub-µm-sized Ca-Ti-rich oxide grains (possibly perovskite), which are set inside hibonite. In addition to the Ca-Ti-rich phase, the assemblage in Fig. 5c contains two sub-µm-sized grains rich in zirconium located at the grain boundary between hibonite and two Ca-Ti-rich oxide grains. Another assemblage occurs close to the lower left side of 2–6–1 (left edge of the CAI and surrounding an interior hole; Fig. 5a), and consists of oxide and silicate mineral layers. The first layer directly adjacent to interior grossite consists of small hibonite platelets (up to ~5 µm across) followed by a discontinuous spinel layer and anorthite (Fig. 5a, b, and d).

3.1.2. Mineral chemistry

Hibonite grains in the studied CAIs have variable MgO and TiO_2 contents (Table 1). Hibonites in 2–5–1 and 2–6–6 have low MgO and TiO_2 contents (~0.2 and 0.4 wt%, respectively); 1–9–1, 1–10–3, and 2–8–7 have intermediate MgO contents of ~0.5 wt%; and platy hibonite crystals 2–2–1 and 2–8–3 have the highest MgO and TiO_2 contents (~1 and 2 wt%, respectively; Table 1). Electron microprobe analyses collected in hibonite grains 2–2–1, 2–6–6, and 2–8–3 suggest that the edges of these hibonite grains are more MgO- and TiO_2-rich than the centers. The elemental maps of 2–8–3 also show center to edge zoning in MgO, TiO_2 and Al_2O_3 (Fig. 6).

EPMA and SEM-WDS analyses of CAI 2–6–1 suggest that both grossite and hibonite (measured in assemblage 1) are close to endmember compositions. Neither of these minerals contains detectable MgO, but titanium was detected at low levels in both (Table 1). While overlap with the surrounding titanium-rich phase cannot be excluded for the hibonite analysis due to its small size, the analysis regions within grossite were free of inclusions. This suggests that titanium is present inside the grossite lattice, and may be trivalent and substituting for Al^{3+}.

The compositions of the RMNs in 2–5–1 and 2–6–6 were reported in Schwander et al. (2015). They are almost entirely composed of iridium, osmium, and ruthenium. They therefore are more refractory than typical RMNs (Schwander et al., 2015), and also are highly depleted in tungsten and molybdenum, which are more volatile under oxidizing compositions (Palme et al., 1998).

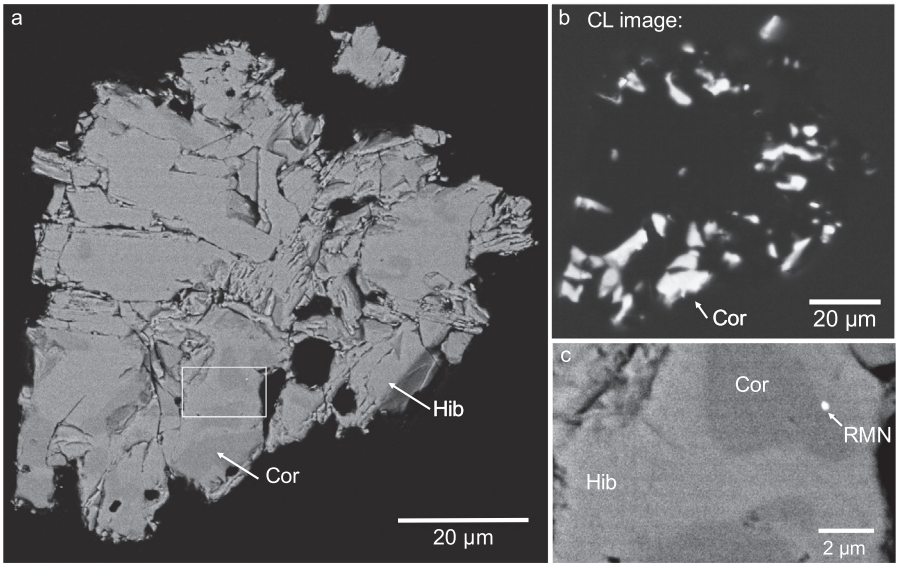

Fig. 4. Hibonite-corundum CAI 1–10–3. (a) The BSE image shows that 1–10–3 is a hibonite aggregate with inclusions of corundum. This image was previously published by Schwander et al. (2015). (b) Corundum shows bright cathodoluminescence (CL); hibonite and epoxy are black. The CL image was obtained with a Hitachi S-3400 SEM equipped with a Gatan PanaCL/F system at the University of Wisconsin, Madison. (c) The enlargement of the white box in (a) shows a refractory metal nugget at a grain boundary between hibonite and corundum. Abbreviations: Hib – hibonite, Cor – corundum, RMN – refractory metal nugget.

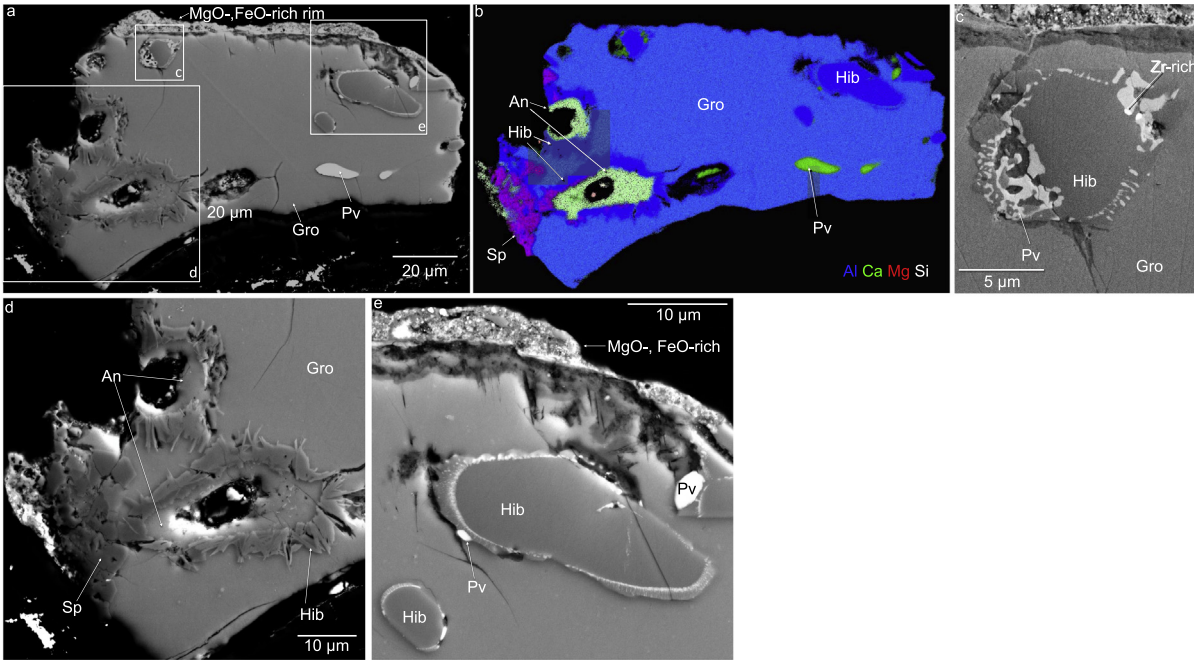

Fig. 5. Grossite-rich CAI 2–6–1 in BSE and EDS false-colors. (a) BSE image. This CAI consists mostly of grossite and is surrounded by a discontinuous FeO-rich rim. (b) Combined elemental map (Mg: red, Ca: green, Al: blue, Si: white) of the CAI. (c) Enlargement of the box labeled 'c' in (a). (d) Enlargement of the box labeled 'd' in (a). (e) Enlargement of the box labeled 'e' in (a). Abbreviations: An –anorthite, Gro – grossite, Hib – hibonite, Pv – perovskite, Sp – spinel. (For interpretation of the references to color in this figure legend, the reader is referred to the web version of this article.)

Table 1
Chemical compositions of the fractionated CAIs obtained by EPMA. Uncertainties correspond to two standard deviations.

					Ions per formula unit						Weight percents					
Name	Phase	Location	# of analyses	Voltage (kV)	Ca^{2+}	Al^{3+}	Mg^{2+}	Ti^{4+}	O^{2-}	Cation sum	CaO (wt%)	Al_2O_3 (wt%)	MgO (wt%)	TiO_2 (wt%)	FeO (wt%)	Sum (wt%)
EPMA																
1–9–1	Hib		1	20	1.016	11.760	0.087	0.117	19	12.993	8.56	90.12	0.53	1.41	b.d.	100.61
1–10–3	Hib		7	15 & 20	0.999	11.820	0.080	0.083	19	12.997	8.39 ± 0.26	90.30 ± 1.85	0.48 ± 0.10	0.99 ± 0.22	b.d.	100.16
2–2–1	Hib	Center	1	20	1.015	11.705	0.140	0.140	19	13.001	8.54	89.48	0.85	1.68	b.d.	100.54
2–2–1	Hib	Edge	1	20	1.024	11.678	0.153	0.149	19	13.004	8.56	88.77	0.92	1.78	b.d.	100.03
2–5–1	Hib	Center	1	20	1.015	11.912	0.026	0.034	19	12.987	8.57	91.44	0.16	0.41	b.d.	100.57
2–5–1	Hib	Center	1	20	1.021	11.909	0.027	0.034	19	12.990	8.63	91.48	0.16	0.41	b.d.	100.67
2–5–1	Hib	Edge	1	20	1.021	11.905	0.030	0.034	19	12.990	8.56	90.69	0.18	0.40	b.d.	99.84
2–5–1	Hib	Edge	1	20	1.008	11.902	0.032	0.035	19	12.977	8.57	91.99	0.20	0.42	b.d.	101.18
2–5–1	Hib	Edge	1	20	1.022	11.909	0.027	0.031	19	12.989	8.63	91.47	0.17	0.37	b.d.	100.63
2–6–1	Gro		3	20	0.997	3.971		0.021	7	4.989	21.54 ± 0.07	78.02 ± 0.41	b.d.	0.64 ± 0.02	b.d.	100.19
2–6–6	Hib	Center	1	20	1.025	11.922	0.032	0.017	19	12.997	8.64	91.31	0.20	0.21	b.d.	100.35
2–6–6	Hib	Center	1	20	1.010	11.925	0.033	0.021	19	12.990	8.56	91.94	0.20	0.26	b.d.	100.96
2–6–6	Hib	Center	1	20	1.017	11.925	0.033	0.019	19	12.994	8.63	91.96	0.20	0.23	b.d.	101.02
2–6–6	Hib	Edge	1	20	1.019	11.871	0.050	0.046	19	12.986	8.53	90.42	0.30	0.55	b.d.	99.80
2–8–3	Hib	Center	1	20	1.004	11.714	0.139	0.141	19	12.998	8.47	89.84	0.84	1.70	b.d.	100.85
2–8–3	Hib	Center	1	15	1.015	11.719	0.139	0.130	19	13.002	8.49	89.08	0.84	1.54	b.d.	99.95
2–8–3	Hib	Edge	1	20	1.005	11.649	0.170	0.172	19	12.995	8.46	89.12	1.03	2.06	b.d.	100.67
2–8–3	Hib	Edge	1	15	1.034	11.638	0.168	0.158	19	12.998	8.54	87.37	1.00	1.85	b.d.	98.76
2–8–3	Hib	Edge	1	15	1.027	11.642	0.168	0.163	19	13.000	8.55	88.07	1.01	1.93	b.d.	99.55
2–8–3	Hib	Edge	1	20	0.998	11.652	0.170	0.174	19	12.993	8.39	89.12	1.03	2.08	b.d.	100.62
2–8–7	Hib	Center	1	20	1.006	11.892	0.059	0.039	19	12.995	8.46	90.93	0.36	0.46	b.d.	100.21
2–8–7	Hib	Edge	1	20	1.005	11.886	0.063	0.043	19	12.997	8.47	91.03	0.38	0.51	b.d.	100.39
SEM with WDS:																
2–6–1	Gro		5	15	1.032	3.954		0.020	7	5.006	22.15 ± 0.32	77.12 ± 1.13	b.d	0.58 ± 0.12		99.85
2–6–1	Hib		3	15	1.057	11.923		0.030	19	13.010	8.72 ± 0.17	89.38 ± 0.94	b.d	0.35 ± 0.03		98.45

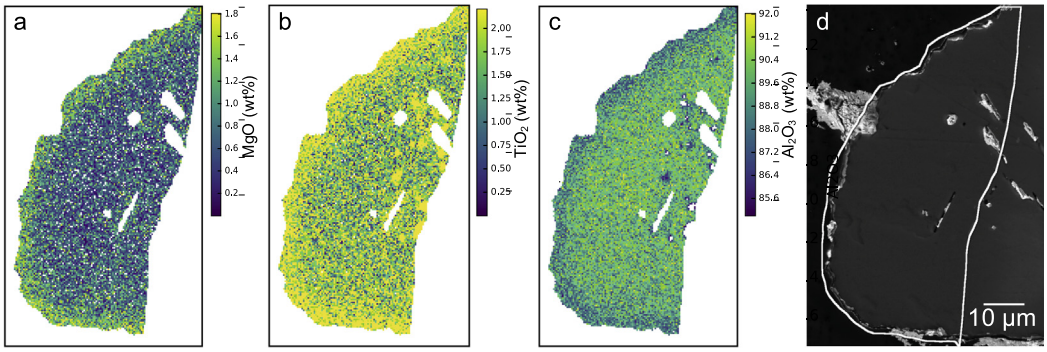

Fig. 6. Elemental zoning in platy hibonite 2–8–3. (a) and (b) show that the grain is zoned in MgO and TiO_2, with the edges of the hibonite being more enriched in MgO and TiO_2 than the center. (c) The edges of the grain are less Al_2O_3-rich than the center. (d) A BSE image of 2–8–3 with the mapped area outlined in white. The mapped area was constrained to one side of the CAI in order to avoid areas of the grain that were charging due to laser beam damage of the coating (laser beam analyses were performed after the isotopic analyses presented here were collected).

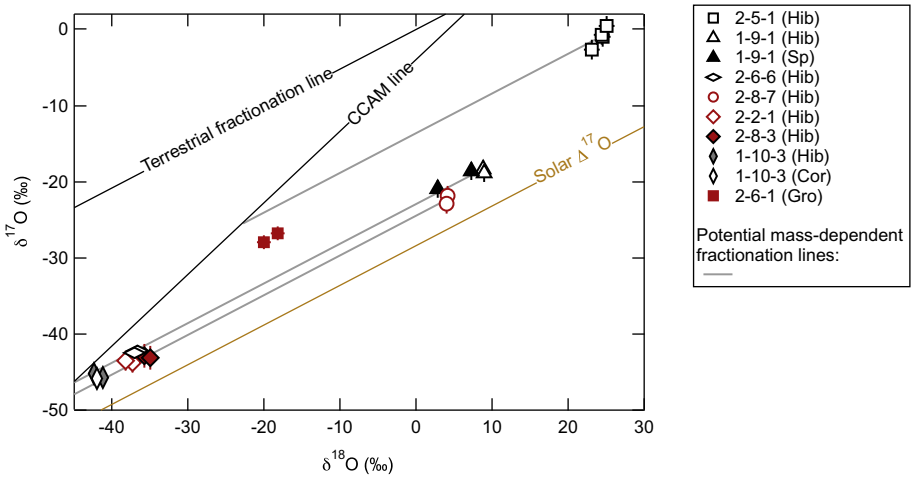

Fig. 7. Oxygen three-isotope plot showing SIMS spot analyses for the eight CAIs. The listed phases (Hib: hibonite, Sp: spinel, Cor: corundum, Gro: grossite) correspond to the analyzed minerals in the CAIs. The solar $\Delta^{17}O$ line refers to the Genesis mission value of ~–28‰ (McKeegan et al., 2011). Plotted uncertainties are 2σ.

3.2. Oxygen isotopes

In the oxygen three-isotope diagram, all eight CAIs plot to the right of the CCAM (carbonaceous chondrite anhydrous mineral) line (Fig. 7). The largest offsets from the CCAM line are shown by spinel-hibonite platelet 1–9–1 and stubby hibonite crystals 2–5–1 and 2–8–7. In comparison, the offsets are small for the hibonite-corundum aggregate 1–10–3, stubby hibonite crystal 2–6–6, platy hibonite crystals 2–2–1 and 2–8–3, as well as grossite-rich CAI 2–6–1. Spot analyses collected inside the same CAI typically agree within measurement uncertainties, only the spot analyses collected in spinel-hibonite platelet 1–9–1 show a larger spread (i.e., one spinel analysis plots closer to the CCAM line than the two hibonite analyses; Fig. 7, Table 2).

Six of the CAIs have $\Delta^{17}O$ values ($\Delta^{17}O = \delta^{17}O - \delta^{18}O \times 0.52$, i.e., a measure for the mass-independent variation in oxygen isotopes) that agree within uncertainty; the average for these six CAIs is -23.8 ± 0.5‰ (uncertainty is 2SE). CAIs 2–5–1 and 2–6–1 have higher $\Delta^{17}O$ values (i.e., -13.6 ± 1.0‰ and -17.4 ± 0.8‰, respectively).

3.3. Magnesium isotopes

The magnesium isotopic analyses obtained in spinel-hibonite platelet 1–9–1 and stubby hibonites 2–6–6 and 2–5–1 fall on a mass-fractionation line of slope ~0.5 drawn through the origin of the magnesium three-isotope diagram (Fig. 8a). With $\delta^{25}Mg$ and $\delta^{26}Mg$ values of ~6–7‰ and ~12–15‰, respectively, CAI 2–6–6 shows the largest correlated excesses. The spinel and one hibonite analysis of CAI 1–9–1 plot close to the origin (Fig. 8a, Table 3), another hibonite analysis has a negative $\delta^{25}Mg$. Stubby hibonite 2–8–7 and platy hibonites 2–2–1 and 2–8–3 have positive $\delta^{26}Mg$, but lack corresponding effects in ^{25}Mg ($\delta^{25}Mg \sim (-5$ to $0)$‰; Fig. 8a).

Consequently, CAIs 2–2–1, 2–8–3, and 2–8–7 have resolved positive $\delta^{26}Mg^*$ values (~10‰, ~40‰, and 45‰,

Table 2
Oxygen isotopic compositions of the eight fractionated CAIs. Uncertainties are 2σ.

Name	Type[a]	Spot[b]	$\delta^{18}O$ (‰)	$\delta^{17}O$ (‰)	$\Delta^{17}O$ (‰)
1–9–1	Platy w. sp	sp1.1	7.23 ± 0.52	−18.65 ± 1.19	−22.40 ± 1.00
		sp1.2	2.81 ± 0.52	−20.92 ± 1.19	−22.39 ± 1.00
		hib1.1	8.76 ± 0.52	−18.34 ± 1.19	−22.90 ± 1.00
		hib1.2	8.98 ± 0.52	−18.87 ± 1.19	−23.53 ± 1.00
1–10–3	Cor-hib aggr.	hib1.1	−41.22 ± 0.74	−45.71 ± 0.56	−24.28 ± 0.48
		hib2.1	−42.45 ± 0.74	−45.16 ± 0.56	−23.09 ± 0.48
		cor1.1	−41.98 ± 0.74	−45.82 ± 0.56	−24.00 ± 0.48
2–2–1	Platy	hib1.1	−37.31 ± 0.68	−43.83 ± 1.31	−24.43 ± 1.40
		hib1.2	−38.23 ± 0.68	−43.55 ± 1.31	−23.67 ± 1.40
2–5–1	Stubby	hib1.1	25.01 ± 1.10	0.44 ± 1.30	−12.56 ± 1.02
		hib1.2	23.15 ± 1.10	−2.68 ± 1.30	−14.72 ± 1.02
		hib1.3	24.48 ± 1.10	−0.93 ± 1.30	−13.65 ± 1.02
		hib1.4	24.36 ± 1.10	−0.73 ± 1.30	−13.40 ± 1.02
2–6–6	Stubby	hib1.1	−36.64 ± 0.71	−42.21 ± 0.80	−23.16 ± 0.85
		hib1.2	−37.02 ± 0.71	−42.48 ± 0.80	−23.22 ± 0.85
2–8–3	Plate	hib1.1	−35.81 ± 0.50	−42.86 ± 1.56	−24.24 ± 1.38
		hib1.2	−34.95 ± 0.50	−43.09 ± 1.56	−24.91 ± 1.38
2–8–7	Stubby	hib1.1	4.08 ± 0.68	−21.89 ± 1.31	−24.01 ± 1.40
		hib1.2	4.04 ± 0.68	−22.90 ± 1.31	−25.00 ± 1.40
2–6–1	Gro-rich	gro1.1	−18.25 ± 0.97	−26.81 ± 0.87	−17.32 ± 0.95
		gro1.2	−20.04 ± 0.97	−27.93 ± 0.87	−17.50 ± 0.95

[a] Petrologic type, abbreviations: aggr. – aggregate, sp – spinel, w. – with, cor – corundum, gro – grossite. If unclear: morhology not recognizable from polished surface.
[b] Notation indicates phase, grain, and spot number, e.g. hib2.1 is the first spot collected on the second analyzed hibonite grain.

respectively; Table 3). Model isochrons yield initial $^{26}Al/^{27}Al$ ratios of $(0.348 \pm 0.058) \times 10^{-5}$ for 2–8–7, $(4.72 \pm 0.27) \times 10^{-5}$ for 2–8–3, and $(4.95 \pm 0.26) \times 10^{-5}$ for 2–2–1. Stubby hibonites 2–6–6 and 2–5–1 as well as spinel-hibonite platelet 1–9–1 lack radiogenic $^{26}Mg^{*}$ excesses (Fig. 8b). The disparity in $^{27}Al/^{24}Mg$ ratios for repeated analyses in stubby hibonite 2–6–6 in Fig. 8b is evidence for strong elemental zoning in this grain.

In CAI 2–6–1, only grossite could be analyzed. The calculated $\delta^{26}Mg^{*}$ value is approximately 3,500,000‰ ($^{26}Mg/^{24}Mg$ ratio of ~482), counting statistics yield a 2σ uncertainty of ~45,000‰. The $^{27}Al/^{24}Mg$ ratio is $\sim(1.02 \pm 0.01) \times 10^{7}$ (corrected using the RSF determined from Madagascar hibonite), which yields a model $^{26}Al/^{27}Al$ ratio of $(4.7 \pm 0.6) \times 10^{-5}$. To the best of our knowledge, the ^{26}Mg excess and the $^{27}Al/^{24}Mg$ ratio in grossite-rich CAI 2–6–1 are the highest ever reported for CAI minerals. For comparison, $^{27}Al/^{24}Mg$ ratios between 70 and 4000 were reported for grossite in CAIs from CR chondrites by Makide et al. (2009), who also corrected the ratios using an RSF obtained from Madagascar hibonite. The ratios reported for the MgO-poor hibonite grains in HAL and H030 (i.e., $^{27}Al/^{24}Mg$ $\sim(1–4) \times 10^{4}$ for HAL, Fahey et al., 1987, and $\sim(0.8–6) \times 10^{4}$ for H030, Rout et al., 2009) and for corundum grains ($^{27}Al/^{24}Mg$ up to $\sim1.4 \times 10^{5}$ in 1769–9–1; Makide et al., 2013) are also lower than in 2–6–1.

3.4. Calcium and titanium isotopes

All studied CAIs are mass-dependently enriched in heavy calcium isotopes (expressed as a positive F_{Ca} value in ‰/amu; for a definition, see Section 2); evidence for fractionation effects in titanium (i.e., F_{Ti} resolved from 0) was only found in some of the CAIs (Table 4). Five CAIs have similarly large F_{Ca} values of ~15‰/amu: platy hibonites 2–2–1 and 2–8–3, spinel-hibonite-platelet 1–9–1, stubby hibonite 2–8–7, and grossite-rich CAI 2–6–1. Smaller F_{Ca} values are found in stubby hibonites 2–5–1 (~10‰/amu) and 2–6–6 (~4‰/amu), and hibonite-corundum aggregate 1–10–3 (~3‰/amu). Resolved fractionation effects in titanium are found in 1–9–1, 2–5–1, and 2–8–7, regardless of normalization. CAIs 1–10–3 and 2–6–6 have small positive F_{Ti} values when normalized to ^{48}Ti, but lack resolved effects when normalized to ^{47}Ti. No or only marginally resolved fractionation effects in titanium were found in grossite-rich CAI 2–6–1 and platy hibonite grains 2–2–1 and 2–8–3 (Table 4).

Mass-independent effects are most pronounced in the neutron-rich isotopes of calcium and titanium, i.e., ^{48}Ca

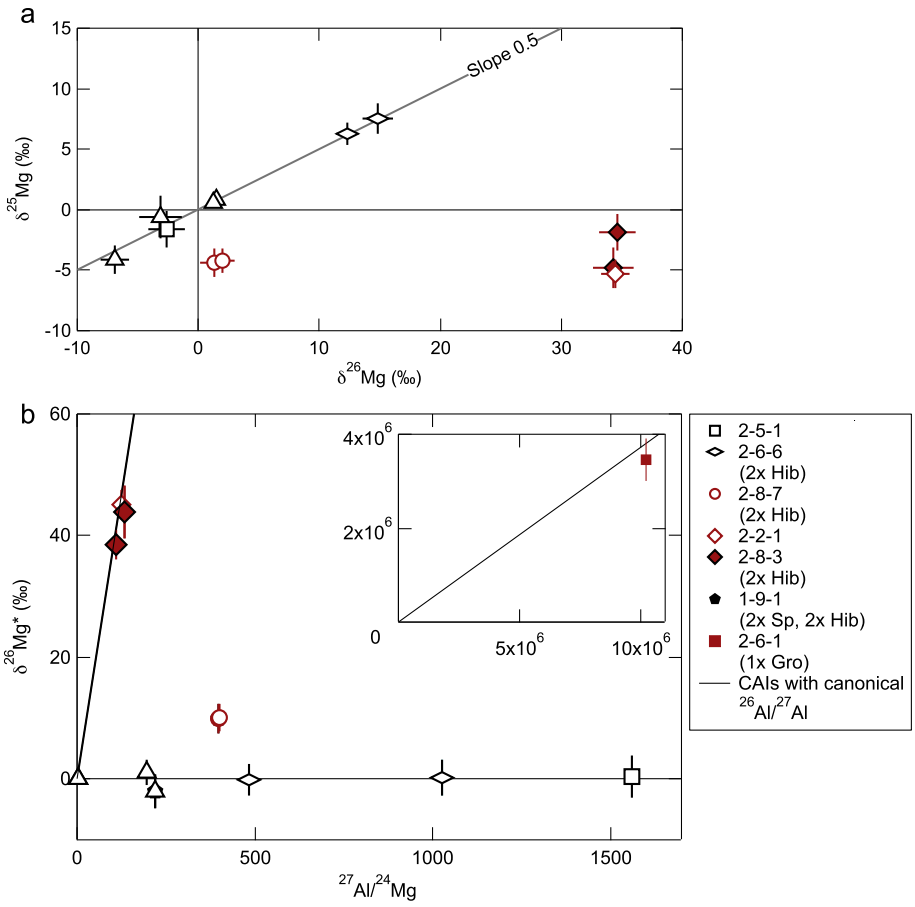

Fig. 8. (a) Magnesium three-isotope plot showing SIMS spot analyses for six of the eight fractionated CAIs. (b) Platy hibonites 2–2–1 and 2–8–3 have positive $\delta^{26}Mg^*$ values consistent with incorporation of ^{26}Al close to the canonical level. In contrast, no evidence for incorporation of live ^{26}Al was found in stubby hibonites 2–6–6 and 2–5–1 as well as spinel-hibonite platelet 1–9–1. The two analyses in stubby hibonite 2–8–7 reveal positive $\delta^{26}Mg^*$ values, consistent with incorporation of ^{26}Al at a subcanonical level. The inset shows the analysis in the grossite-rich CAI 2–6–1, which has an extremely high $^{27}Al/^{24}Mg$ ratio and cannot be plotted on the same scale. Plotted uncertainties are 2σ.

and ^{50}Ti (Fig. 9). Anomalies in ^{48}Ca are resolved in four CAIs (Table 4). These are stubby hibonites 2–5–1 ($\delta^{48}Ca \sim 40‰$) and 2–6–6 ($\delta^{48}Ca \sim 10‰$), spinel-hibonite platelet 1–9–1 ($\delta^{48}Ca \sim 10‰$), and hibonite-corundum aggregate 1–10–3 ($\delta^{48}Ca \sim -15‰$). Anomalies in ^{50}Ti tend to be smaller than in ^{48}Ca and the magnitudes depend on the normalizing isotope pair. No effects are resolvable beyond a 3σ-uncertainty in $^{49}Ti/^{47}Ti$ normalization, but stubby hibonite 2–5–1 shows a resolved ^{50}Ti excess in $^{46}Ti/^{48}Ti$ normalization (Table 4).

4. DISCUSSION

4.1. Classification

All studied CAIs are isotopically heavy in calcium isotopes. Such enrichments are usually attributed to evaporative loss from highly refractory melts (Ireland et al., 1992; Floss et al., 1996). This calcium isotope fractionation further justifies a classification of these CAIs as FUN or F CAIs, even though many of them lack mass-fractionation effects in magnesium. The common definition for FUN CAIs, which includes the presence of significant fractionation in magnesium isotopes (as summarized by MacPherson, 2014), does not seem applicable for the most refractory examples of F(UN) CAIs, as many, including the famous FUN CAI HAL, lack fractionation effects in magnesium (Lee et al., 1979; Fahey et al., 1987). This is likely because magnesium was completely lost during evaporation and isotopically normal magnesium was reintroduced at a later stage (Ireland et al., 1992; see Section 4.4).

Therefore, stubby hibonite 2–5–1 and spinel-hibonite platelet 1–9–1 can be classified as FUN CAIs, as they have considerable nucleosynthetic anomalies and large fractionation effects in calcium, titanium and oxygen. Hibonite-corundum aggregate 1–10–3 and stubby hibonite 2–6–6 have smaller, but clearly resolved fractionation effects in calcium (2–6–6 is also fractionated in magnesium isotopes) and clear enrichments in ^{48}Ca; they should thus also be grouped with the FUN CAIs. The remaining CAIs, 2–8–7, 2–2–1, 2–8–3, and 2–6–1, have no mass-independent anomalies in calcium and titanium isotopes, which suggests a classification as F CAIs.

Table 3
Aluminum-magnesium isotopic compositions of seven of the eight fractionated CAIs. Uncertainties are 2σ.

Name	Type[a]	Spot[b]	Session[c]	Cycles[d]	Standard[e]	$\delta^{25}Mg$ (‰)	$\delta^{26}Mg$ (‰)	$^{27}Al/^{24}Mg$	$\delta^{26}Mg^{*}$ (‰)	$^{26}Al/^{27}Al$ (10^{-5}) Model[f]	$^{26}Al/^{27}Al$ (10^{-5}) Internal[g]
1–9–1	Platy w. sp	hib1.1	Feb14	39	An 1% MgO	-0.57 ± 1.79	-3.10 ± 1.79	220.90 ± 2.89	-1.98 ± 2.73	-0.12 ± 0.17	-0.01 ± 0.11
		hib1.2	July14	39	An 1% MgO	-4.13 ± 1.16	-6.90 ± 1.16	194.97 ± 2.52	1.14 ± 2.13	0.08 ± 0.15	
		sp1.1	July14	30	Sp	0.79 ± 0.14	1.53 ± 0.25	2.61 ± 0.03	-0.01 ± 0.14		
		sp1.2	July14	30	Sp	0.61 ± 0.14	1.17 ± 0.25	2.64 ± 0.03	-0.02 ± 0.14		
2–2–1	Platy	hib1.1	July14	39	An 1% MgO	-5.25 ± 1.16	34.50 ± 1.16	125.83 ± 1.60	44.71 ± 2.35	4.95 ± 0.26	
2–5–1	stubby	hib1.1	Feb14	39	An 0.1% MgO	-1.56 ± 1.50	-2.57 ± 1.50	1560.67 ± 15.91	0.47 ± 3.50	0.00 ± 0.03	
2–6–6	Stubby	hib1.1	Feb14	39	An 0.1% MgO	7.48 ± 1.33	14.80 ± 1.33	1026.38 ± 10.67	0.14 ± 2.99	0.00 ± 0.04	
		hib1.2	Feb14	39	An 0.1% MgO	6.30 ± 0.91	12.29 ± 0.91	484.24 ± 5.06	-0.05 ± 2.50	0.00 ± 0.07	
2–8–3	Platy	hib1.1	Feb14	36	An 1% MgO	-4.76 ± 1.66	34.30 ± 1.66	134.23 ± 4.73	43.56 ± 4.34	4.52 ± 0.48	
		hib1.2	Feb14	39	An 1% MgO	-1.87 ± 1.46	34.57 ± 1.46	110.58 ± 1.74	38.20 ± 2.47	4.81 ± 0.32	
2–8–7	Stubby	hib1.1	Feb14	39	An 0.1% MgO	-4.43 ± 1.17	1.28 ± 1.17	397.78 ± 4.29	9.87 ± 2.37	0.35 ± 0.08	
		hib1.2	Feb14	39	An 0.1% MgO	-4.18 ± 0.97	1.97 ± 0.97	400.55 ± 4.22	10.08 ± 2.31	0.35 ± 0.08	
2–6–1		gro1.1	July14	21	see text			$1.02 \times 10^{7} \pm 1 \times 10^{5}$	$(3.46 \pm 0.45) \times 10^{6}$	4.73 ± 0.62	

[a] Petrologic type with abbreviations as in Table 1.
[b] Phase analyzed.
[c] SIMS analysis session.
[d] Number of cycles included in average.
[e] Standard used for correction of instrumental fractionation. 'An 1% MgO' and 'An 0.1% MgO' refer to synthetic anorthite standards with 1 and 0.1 wt% MgO, respectively.
[f] Inferred from model isochron.
[g] Inferred from internal isochron.

Table 4
Calcium and titanium isotopic compositions of the eight fractionated CAIs. Titanium data is given in two commonly used normalizations ($^{46}Ti/^{48}Ti$ normalization is preferred, $^{49}Ti/^{47}Ti$ normalization (italics) is given to facilitate comparison with other recent studies). Uncertainties are 2σ.

Name	Type[a]	Analyzed phases[b]	$\delta^{47}Ti$ (‰)	$\delta^{49}Ti$ (‰)	$\delta^{50}Ti$ (‰)	F_{Ti}[c] (‰/amu)	$\delta^{46}Ti$ (‰)	$\delta^{48}Ti$ (‰)	$\delta^{50}Ti$ (‰)	F_{Ti} (‰/amu)	$\delta^{42}Ca$ (‰)	$\delta^{43}Ca$ (‰)	$\delta^{48}Ca$ (‰)	F_{Ca} (‰/amu)
			$^{46}Ti/^{48}Ti$ normalization[d]:				$^{49}Ti/^{47}Ti$ normalization:				$^{40}Ca/^{44}Ca$ normalization:			
1–9–1	Platy w. sp	Hib, Pv (minor)	0.6 ± 2.3	0.5 ± 2.5	2.9 ± 3.2	3.8 ± 1.0	*−0.7 ± 2.8*	*−0.5 ± 2.5*	*2.6 ± 5.4*	*3.6 ± 1.4*	1.7 ± 3.1	1.7 ± 2.8	14.1 ± 5.4	14.7 ± 0.6
1–10–3	Aggr. w. cor	Hib	−1.9 ± 2.8	−3.3 ± 3.0	4.5 ± 3.4	2.4 ± 1.1	*1.3 ± 3.5*	*2.6 ± 3.0*	*8.6 ± 5.7*	*1.6 ± 1.7*	−2.3 ± 2.5	−3.9 ± 3.1	−14.0 ± 4.5	3.3 ± 0.9
2–2–1	Platy	Hib	−2.1 ± 5.1	0.0 ± 4.1	6.0 ± 6.9	−0.7 ± 3.3	*3.7 ± 4.3*	*0.8 ± 4.7*	*4.3 ± 9.2*	*0.6 ± 2.6*	−0.8 ± 3.0	0.6 ± 2.6	−0.3 ± 6.6	15.6 ± 0.4
2–5–1	Stubby	Hib	−1.2 ± 4.0	5.4 ± 4.5	14.1 ± 5.8	8.9 ± 1.8	*3.6 ± 4.3*	*−2.0 ± 4.2*	*5.2 ± 8.7*	*12.2 ± 2.4*	5.4 ± 2.3	3.9 ± 3.6	42.7 ± 5.3	10.0 ± 0.5
2–6–6	Stubby	Hib, RMN (minor)	2.5 ± 3.8	0.9 ± 4.1	3.9 ± 5.6	3.2 ± 1.7	*−4.2 ± 4.1*	*−0.7 ± 3.8*	*6.3 ± 7.0*	*1.4 ± 1.9*	1.8 ± 4.8	0.6 ± 2.8	13.8 ± 4.1	4.2 ± 1.0
2–8–3	Platy	Hib	0.7 ± 2.2	1.3 ± 2.5	4.2 ± 3.2	0.7 ± 1.0	*0.1 ± 2.7*	*−0.9 ± 2.5*	*2.4 ± 5.1*	*1.2 ± 1.4*	−1.4 ± 2.3	0.4 ± 3.5	0.1 ± 5.1	16.7 ± 0.5
2–8–7	Stubby	Hib, RMN (minor)	1.3 ± 3.9	−0.1 ± 4.2	−3.8 ± 5.7	12.1 ± 1.6	*−1.9 ± 4.4*	*−0.4 ± 4.2*	*−2.2 ± 7.7*	*11.4 ± 2.2*	−0.3 ± 4.9	1.0 ± 2.9	−2.5 ± 4.3	15.6 ± 0.9
2–6–1	Gro-rich	Gro	−0.7 ± 3.4	−1.8 ± 3.9	4.8 ± 4.9	2.0 ± 1.8	0.3 ± 4.3	1.2 ± 3.5	7.2 ± 6.5	1.5 ± 1.8	0.1 ± 2.6	−1.5 ± 3.0	−2.8 ± 4.1	15.6 ± 0.9

[a] Petrologic type with abbreviations as in Table 2.
[b] Analyzed phases as found in analysis pit post SIMS. Minor indicates that the relative contribution of the second listed mineral was small. Abbreviations: Hib – hibonite, Pv – perovskite, RMN – refractory metal nugget, Gro – grossite.
[c] Intrinsic fractionation in Ti.
[d] Favored normalization for Ti isotopes.

The FUN CAIs (1–9–1, 2–5–1, 2–6–6) measured for magnesium isotopes show no evidence for incorporation of live ^{26}Al. In contrast, the four F CAIs (2–2–1, 2–6–1, 2–8–3, 2–8–7) show indications for incorporation of live ^{26}Al. However, while 2–2–1, 2–8–3, and 2–6–1 have model $(^{26}Al/^{27}Al)_0$ ratios close to canonical, 2–8–7 has a low model $(^{26}Al/^{27}Al)_0$ of $\sim 3 \times 10^{-6}$ that is similar to the ratios found in some FUN CAIs (e.g., C1, DH-H1; Krot et al., 2014b; Park et al., 2017; and references therein). 2–8–7 may therefore be closer related to FUN CAIs rather than F CAIs, its lack of resolved anomalies could simply be a coincidence as anomalies in ^{48}Ca and ^{50}Ti in FUN CAIs span a range from negative to positive values. We do not expect that Al-Mg systematics in hibonite were affected by parent body processing.

4.2. Individual isotopic systems

4.2.1. Oxygen isotopes

All studied CAIs are offset to the right of the CCAM line. We quantify this offset using the $\Delta^{18}O_{CCAM}$ value, which is the deviation from the line in $\delta^{18}O$ ($[\Delta^{18}O_{CCAM} = \delta^{18}O + (\Delta^{17}O - Intercept_{CCAM})/(Slope_{MFL} - Slope_{CCAM})]$, MFL stands for mass-dependent fractionation line; Kööp et al., 2016b). If the offset from the CCAM line is due to mass-dependent fractionation only, $\Delta^{18}O_{CCAM}$ values can be directly compared to $\delta^{18}O$ values from experimental evaporation studies (e.g., Mendybaev et al., 2013, 2017). Corundum-hibonite aggregate 1–10–3 has the smallest $\Delta^{18}O_{CCAM}$ (~5‰). Platy hibonites 2–2–1 and 2–8–3, and stubby hibonite 2–6–6 have $\Delta^{18}O_{CCAM}$ of ~10‰, which is larger than in SHIBs (Kööp et al., 2016b), but similar to many PLAC-like CAIs (Kööp et al., 2016a). Stubby hibonites 2–5–1 and 2–8–7 as well as spinel-hibonite platelet 1–9–1 have larger $\Delta^{18}O_{CCAM}$ values (~50‰). A mass-dependent fractionation origin (e.g., by incomplete melt evaporation of oxygen) for the offsets is likely, as the individual spinel and hibonite analyses in 1–9–1 fall along a line with slope of ~0.5 (Fig. 7) and the position of these grains in the oxygen three-isotope diagram is similar to F(UN) CAIs (e.g., Krot et al., 2010, 2014b, and references therein).

Most of the studied CAIs have $\Delta^{17}O$ values similar to many other F(UN) and regular CAIs (i.e.,~–23‰ to ~–24‰; Makide et al., 2009; Krot et al., 2010 and references therein, 2014b; Bullock et al., 2012; Kööp et al., 2016b; Kawasaki et al., 2017; Ushikubo et al., 2017; Williams et al., 2017). The only two CAIs with different $\Delta^{17}O$ values are the grossite-rich CAI 2–6–1 and the highly offset stubby hibonite 2–5–1. Both are ^{16}O-poor compared to the other studied hibonite-rich CAIs. Similar or even higher $\Delta^{17}O$ values have been reported for F(UN) CAIs (Krot et al., 2010, 2014b).

4.2.2. Magnesium isotopes and ^{26}Al-^{26}Mg systematics

$\delta^{25}Mg$ values collected in hibonite are negative in almost all studied CAIs. This may in part be the result of having used an anorthite standard for instrumental mass fractionation correction (see Section 2.4.2). We therefore only attribute significance to relative differences within the sample

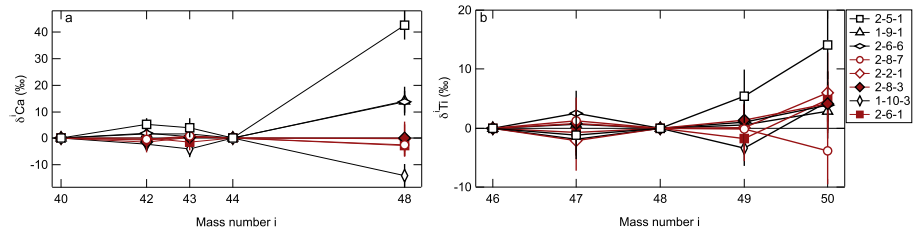

Fig. 9. Calcium (a) and titanium (b) isotopic compositions of the studied hibonite-rich and grossite-rich CAIs. Calcium data is normalized to $^{44}Ca/^{40}Ca$, titanium to $^{46}Ti/^{48}Ti$. Note that anomalies are plotted on different scales in (a) and (b).

set, not to absolute values. The only grain that is clearly mass-dependently enriched in heavy magnesium isotopes relative to the other CAIs is stubby hibonite 2–6–6, which has a $\delta^{25}Mg$ of ~6–7‰/amu (Fig. 8a). The small spread defined by analyses in 1–9–1 (in spinel and hibonite; Fig. 8a) may not be significant, as the analyses were collected in different sessions and the magnitude of $\delta^{25}Mg$ variations is comparable to two analyses collected in platy hibonite crystal 2–8–3, which are not accompanied by corresponding variations in $\delta^{26}Mg$ (Fig. 8a). The lack of large magnesium isotopic fractionation in most studied hibonites is similar to many PLAC-like CAIs and SHIBs (Kööp et al., 2016a,b) as well as HAL-type hibonites (Ireland et al., 1992). In contrast, hibonite grains in multimineralic FUN CAIs often have large mass-dependent Mg fractionation, similar to those observed in other minerals (Holst et al., 2013; Park et al., 2017).

Four CAIs (2–2–1, 2–6–1, 2–8–3, and 2–8–7) show mass-independent ^{26}Mg excesses, three CAIs (1–9–1, 2–5–1, and 2–6–6) show no such ^{26}Mg excesses, and 1–10–3 was not analyzed for magnesium isotopes. Assuming that the ^{26}Mg excesses are due to ^{26}Al decay, the two platy crystals, 2–2–1 and 2–8–3, and grossite-rich CAI 2–6–1 give similar model initial $^{26}Al/^{27}Al$ ratios (i.e., $(4.95 \pm 0.26) \times 10^{-5}$, $(4.72 \pm 0.27) \times 10^{-5}$ and $(4.73 \pm 0.62) \times 10^{-5}$, respectively). All are close to the canonical ratio (Jacobsen et al., 2008) and in excellent agreement with the initial ratio inferred from a multi-SHIB mineral isochron (Kööp et al., 2016b). For 2–6–1, the extreme depletion in the nonradiogenic magnesium isotopes coupled with the large excess of ^{26}Mg may be explained by in-situ ^{26}Al decay in an essentially magnesium-free CAI, e.g., due to a near complete evaporation of magnesium prior to crystallization of the grossite. For 2–8–7, the model initial $^{26}Al/^{27}Al$ ratio, $(3.48 \pm 0.58) \times 10^{-6}$, is lower than in regular CAIs, higher than in the FUN CAI HAL, and similar to some other FUN CAIs (e.g., C1; Esat et al., 1978; Fahey et al., 1987; Park et al., 2017). Since no internal isochrons could be constructed for the single hibonite crystals, the positive $\delta^{26}Mg^*$ cannot be unequivocally ascribed to ^{26}Al decay, as they could also be the result of nucleosynthetic ^{26}Mg or ^{24}Mg excesses. However, the position of the grains in the magnesium three-isotope diagram (Fig. 8a; i.e., all three samples have $\delta^{25}Mg$ values close to 0‰) suggests that the variation is likely in ^{26}Mg (radiogenic or nucleosynthetic), not in ^{24}Mg. The only CAI for which two mineral phases could be analyzed and therefore regression of an internal isochron could have been possible is the spinel-hibonite platelet 1–9–1; however, a fit through two spinel and two hibonite analyses shows no evidence for incorporation of live ^{26}Al: $(^{26}Al/^{27}Al)_0 = <1.0 \times 10^{-6}$.

4.2.3. Calcium and titanium isotopes

All studied CAIs show resolved intrinsic mass-dependent fractionation in calcium isotopes (F_{Ca} between 3 and 16‰/amu). All of these values were corrected for instrumental fractionation using a hibonite bracketing standard. This includes the analysis of CAI 2–6–1, in which grossite was analyzed. Due to the matrix effect, both F_{Ca} and F_{Ti} values could be slightly biased for this CAI, but we do not expect that the high F_{Ca} value of (15.6 ± 0.9)‰/amu is purely the result of the matrix effect for this CAI.

Clear evidence for mass-dependent fractionation (MDF) in titanium isotopes is only present in some of the samples (e.g., 1–9–1, 2–5–1, and 2–8–7). The magnitude of calculated F_{Ti} values depends on the isotope chosen for normalization (compare Fig. 10a and b), which could be a result of mass-independent (e.g., nucleosynthetic) variation in one or more of the isotopes in question. Potential candidates for nucleosynthetic anomalies (aside from known effects in ^{50}Ti) are ^{49}Ti and ^{46}Ti. For the former, variations have been reported in PLACs, which tend to mimic the large-scale anomalies in ^{50}Ti in sign (e.g., Ireland, 1988). If this was the case for the CAIs presented here, it could potentially account for the shift in F_{Ti} for 2–5–1 from lower (MDF assessed using $^{46}Ti/^{48}Ti$; Fig. 10b) to higher values (MDF assessed using $^{49}Ti/^{47}Ti$; Fig. 10a), as this CAI has a positive anomaly in ^{50}Ti (Table 4). Variations in ^{46}Ti have been identified in CV CAIs and were shown to correlate with anomalies in ^{50}Ti (Trinquier et al., 2009; MDF assessed using $^{49}Ti/^{47}Ti$), but such effects were found in neither PLACs or PLAC-like CAIs (Ireland, 1988; Kööp et al., 2016a) nor in the F(UN) CAIs studied here (Table 4). Since the mass-independent isotopic properties of FUN CAIs resemble those of PLACs and PLAC-like CAIs more closely (e.g., presence of both enrichments and depletions in ^{50}Ti, variations in $\Delta^{17}O$; e.g., Ireland, 1988; Kööp et al., 2016a), normalization to $^{46}Ti/^{48}Ti$ is likely more appropriate for the eight CAIs studied here as well. The significance of mass-fractionation effects in calcium and titanium is discussed in Section 4.4.

The range in $\delta^{48}Ca$ is significantly larger than in $\delta^{50}Ti$ for the studied CAIs (−14‰ to +43‰ vs. −4‰ to + 14‰, respectively; Fig. 11). The presence of resolved anomalies in ^{48}Ca and/or ^{50}Ti appears to be limited to CAIs which show no indication for incorporation of live

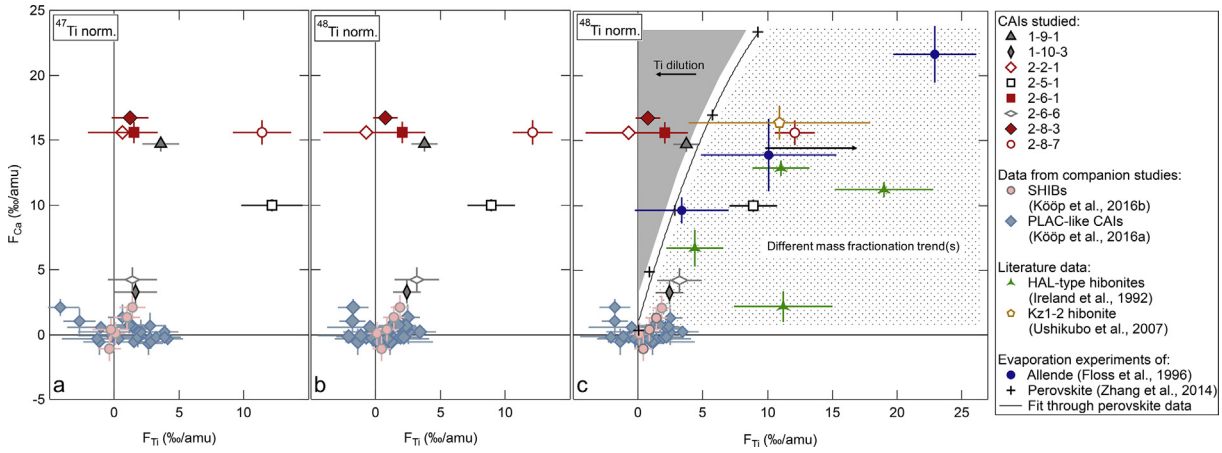

Fig. 10. Comparison of mass-dependent fractionation effects in calcium and titanium. (a) The fractionated CAIs (this study) as well as PLAC-like CAIs and SHIBs, which were studied in the same sessions, are shown. Titanium data is normalized to ^{47}Ti. (b) Shows the titanium data in ^{48}Ti normalization. (c) Shows the same data as (b), as well as data for experimental melt residues and fractionated hibonites described in literature. CAIs in the dotted region may represent compositions that evolved from melts that followed different mass fractionation trends than that found by Zhang et al. (2014). CAIs in the gray area may be affected by dilution with normal titanium (see text for details). Uncertainties are 2σ.

^{26}Al (1–9–1, 2–5–1, and 2–6–6), while CAIs with potential incorporation of ^{26}Al (2–2–1, 2–6–1, 2–8–3, and 2–8–7) show no anomalies beyond 3σ uncertainty. However, no magnesium isotopic data were obtained for corundum-hibonite aggregate 1–10–3, the only CAI with a ^{48}Ca depletion. Similar to mass-fractionation effects, the magnitude of ^{50}Ti anomalies depends on the normalization isotope pair (Fig. 11). For example, the CAI with the largest δ^{48}Ca (~43‰), 2–5–1, lacks a resolvable excess in δ^{50}Ti when normalized to ^{49}Ti/^{47}Ti, but has a resolved δ^{50}Ti excess in ^{46}Ti/^{48}Ti normalization. As discussed above, this effect could be a result of a covariation between ^{49}Ti and ^{50}Ti, which would lead to a decrease in the magnitude of δ^{50}Ti when normalized to ^{49}Ti/^{47}Ti. As the ^{46}Ti/^{48}Ti normalization has been found to be more useful for PLAC-like CAIs and the δ^{48}Ca-δ^{50}Ti distribution closely resemble that found in PLAC-like CAIs with moderate isotopic anomalies (Kööp et al., 2016a), only ^{46}Ti/^{48}Ti normalization is considered in the discussion below.

4.3. Relationships between mass-independent isotope effects

To investigate the relationship between mass-independent effects in different elements (e.g., radiogenic excesses, nucleosynthetic anomalies), we first address the question of whether the elevated δ^{26}Mg* values in four studied CAIs (i.e., platy hibonites 2–2–1 and 2–8–3, grossite-rich CAI 2–6–1, stubby hibonite 2–8–7) are the result of ^{26}Al decay or nucleosynthetic magnesium anomalies. The largest excess in ^{26}Mg was observed in the grossite-rich CAI (δ^{26}Mg* of ~3,500,000‰). A nucleosynthetic anomaly is unlikely due to the large magnitude (for comparison, the largest nucleosynthetic anomalies in materials considered to have formed in the Solar System are on the order of only ~300‰; Ireland, 1990); instead, the excess can be attributed to incorporation of ^{26}Al almost at the canonical level. For the other three CAIs (2–2–1, 2–8–3, and 2–8–7), a radiogenic origin is indicated by three lines of evidence. (1) As argued in Section 4.2.2, the elevated δ^{26}Mg* values are likely due to an excess in ^{26}Mg rather than an excess in ^{24}Mg. (2) The lack of clearly resolved anomalies in calcium and titanium isotopes in all four CAIs suggests that they formed in a well-mixed reservoir. If true, no nucleosynthetic anomalies in magnesium would be expected. (3) The three CAIs have Δ^{17}O values similar to regular ^{26}Al-bearing CAIs and SHIBs (i.e.,~–23‰). This further supports the view that these CAIs formed in an evolved, homogenized reservoir that should not have retained magnesium isotopic heterogeneity on the order that is observed in the three CAIs (compare Kööp et al., 2016a,b). Thus, it seems reasonable to conclude that the elevated δ^{26}Mg* values in stubby hibonite 2–8–7 and the fractionated platy hibonite crystals (2–2–1 and 2–8–3) correspond to incorporation of ^{26}Al at levels of $(0.3 \pm 0.1) \times 10^{-5} \times {}^{27}$Al and $(4.8 \pm 0.2) \times 10^{-5} \times {}^{27}$Al, respectively.

In contrast to the aforementioned CAIs, no evidence for ^{26}Al incorporation was found in fractionated hibonites 2–5–1 and 2–6–6 as well as fractionated spinel-hibonite platelet 1–9–1 (e.g., Fig. 8b). Therefore, it appears that the fractionated CAIs belong to at least three distinct isotopic populations: ^{26}Al-free CAIs, CAIs with intermediate ^{26}Al/^{27}Al, and CAIs with approximately canonical ^{26}Al/^{27}Al. Among the seven CAIs studied for ^{26}Al-^{26}Mg systematics, only the ^{26}Al-free CAIs show anomalies in ^{48}Ca and ^{50}Ti beyond 3σ (Fig. 12). The CAIs are therefore consistent with the mutual exclusivity relationship between resolved anomalies in ^{48}Ca and potentially radiogenic excesses in ^{26}Mg in hibonite-bearing CAIs (Clayton et al., 1988) and a scenario in which ^{26}Al arrived in the CAI formation region after first generations of CAIs had formed and isotopic anomalies had been largely erased or diluted (e.g., Wood, 1998; Sahijpal and Goswami, 1998; Kööp et al., 2016a). If the low ^{26}Al/^{27}Al ratio of (0.348

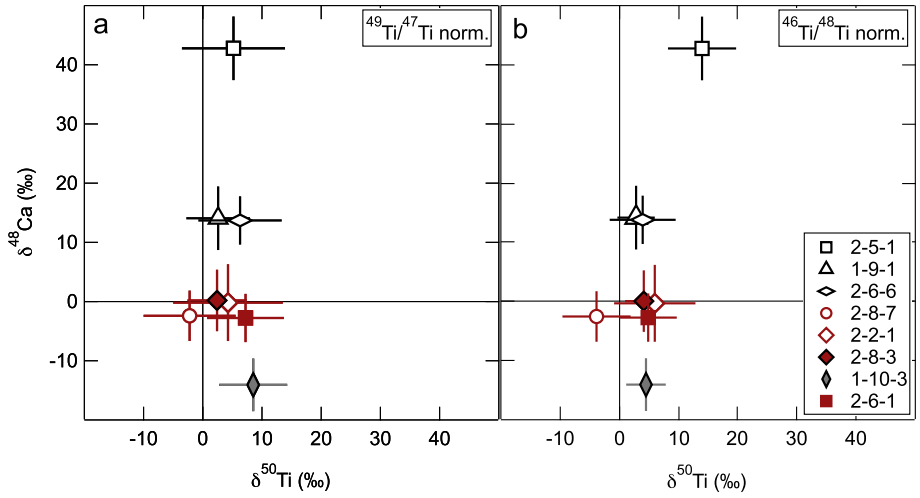

Fig. 11. Comparison of nucleosynthetic anomalies in ^{48}Ca and ^{50}Ti in ^{49}Ti/^{47}Ti (a) and ^{46}Ti/^{48}Ti normalization (b). The range of nucleosynthetic effects is greater in ^{48}Ca than in ^{50}Ti. The magnitude of δ^{50}Ti values depends on the normalization isotopes, as seen for 2–5–1 and 1–10–3 in (a) and (b). Uncertainties are 2σ.

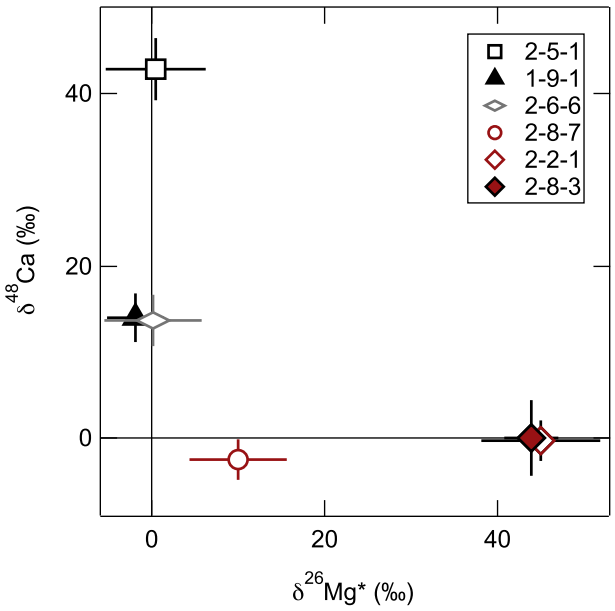

Fig. 12. The FUN and F CAIs show a mutual exclusivity relationship between resolved anomalies in ^{48}Ca and potentially radiogenic excesses in ^{26}Mg. 2–6–1 could not be plotted on this scale, but supports the relationship. Plotted uncertainties are 2σ.

$\pm 0.058) \times 10^{-5}$ in CAI 2–8–7 is due to formation during admixture of ^{26}Al, the lack of resolved anomalies in this CAI could indicate that isotopic heterogeneity had decreased to a level of ≤~5‰ upon admixture of ^{26}Al. Alternatively, if ^{26}Al did not arrive late and was instead homogeneously distributed in the early Solar System, heating mechanisms must have existed late in solar nebula history (at least ~4–5 Ma after CAIs with canonical ratios formed) that reset the ^{26}Al-^{26}Mg system such that no resolved radiogenic ^{26}Mg excesses would be preserved in some of the CAIs. This would likely require complete loss and reintroduction of isotopically normal magnesium (see Section 4.4).

For the fractionated CAIs, anomalies in ^{48}Ca are larger than in ^{50}Ti (Fig. 11) and the most anomalous CAIs are clearly resolved from the correlation line defined by bulk meteorites (Dauphas et al., 2014; Fig. 13). The offsets from the correlation line are similar to those found in PLAC-like CAIs with comparable anomalies in ^{48}Ca ($|\delta| = 0$ to ~50‰), while some PLAC-like CAIs with larger anomalies ($|\delta| >$ ~50‰) show significantly larger offsets (Fig. 13).

The fractionated CAIs studied here show the same relationship between ^{16}O enrichment and the magnitude of anomalies in ^{48}Ca and ^{50}Ti as PLAC-like CAIs: large anomalies are only found in CAIs with Δ^{17}O higher than solar (McKeegan et al., 2011), and the range of δ^{48}Ca and δ^{50}Ti increases with Δ^{17}O (Kööp et al., 2016a). In particular, the highly fractionated stubby hibonite 2–5–1 has the largest anomalies in ^{48}Ca and ^{50}Ti and has the most elevated Δ^{17}O value. As for PLAC-like CAIs, the link between anomalous compositions and oxygen isotopes may be indicative of a ^{16}O-poor character for the reservoir that contained anomalous calcium and titanium carriers (Kööp et al., 2016a).

4.4. Relationship between mass-dependent isotope fractionation in different elements

4.4.1. The problem of the stable isotopic patterns

All studied CAIs show heavy isotope enrichment in calcium (~3–17‰/amu) and some also in titanium (~0–12‰/amu). All have positive $\Delta^{18}O_{CCAM}$ values (~9–53‰), but only three are highly fractionated in oxygen (~50‰). Five of the eight CAIs show no heavy isotope enrichment in magnesium, and only one (2–6–6) is heavy in magnesium (1–10–3 was not analyzed for magnesium isotopes and the degree of fractionation in the grossite in 2–6–1 cannot be assessed due to low magnesium abundances). Mass-dependent heavy isotope enrichments in these elements

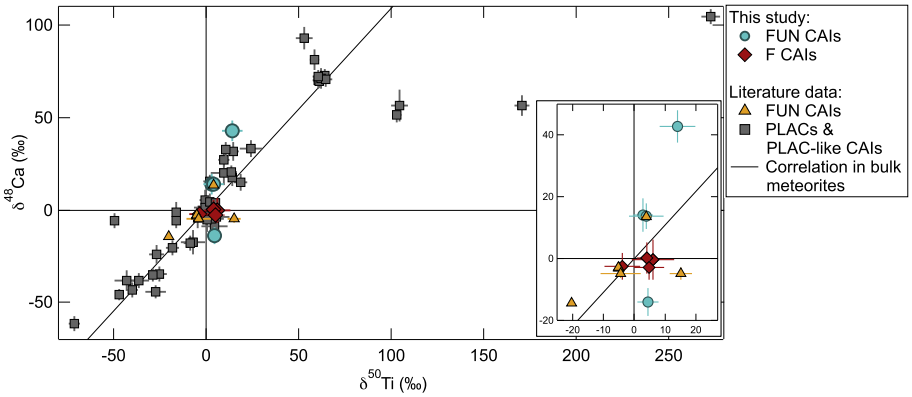

Fig. 13. Comparison of the distribution of δ^{48}Ca and δ^{50}Ti values between F(UN) and UN CAIs (i.e., PLACs and PLAC-like CAIs). FUN and UN CAIs scatter around the correlation line defined by bulk meteorites (extrapolated from Dauphas et al., 2014). The inset shows only FUN CAI data (this study and literature). Literature data for FUN CAIs by CAI name: EK-1–4–1: Niederer et al. (1981); 1623–5: Loss et al. (1994); BG82HB1: Papanastassiou and Brigham (1988); C-1 & BG82DH8: Papanastassiou and Brigham (1987); HAL: Fahey et al. (1987), Ireland et al. (1992). Literature data for PLACs and PLAC-like CAIs: Zinner et al. (1986, 1987), Fahey et al. (1987), Ireland (1990), Sahijpal et al. (2000), Liu et al. (2009) and Kööp et al. (2016a). Plotted uncertainties are 2σ and titanium data is normalized to ^{46}Ti/^{48}Ti.

have been observed in other CAIs and are usually attributed to incomplete evaporation of the element, likely from a melt (Ireland et al., 1992; Floss et al., 1996; Mendybaev et al., 2013; Krot et al., 2014b, and references therein, Park et al., 2017). The problem with the results established here is that they are in conflict with experimental constraints and theoretical considerations (see problems 1–4 outlined below) and seem to imply a decoupling between mass-dependent fractionation effects in different elements. It is unlikely that this is due to errors in the correction for instrumental effects, as the CAIs were analyzed alongside a large number of other hibonite-rich CAIs for which no comparable effects were found (Kööp et al., 2016a,b). Therefore, the effects are considered to be real and intrinsic to the CAIs studied. In the discussion below, it is generally assumed that the precursors of the CAIs were initially solid (i.e., solar nebula condensates, primordial dust or mixtures thereof) and that the CAIs are the residues of melt evaporation from those precursors.

Problem (1): All studied CAIs are isotopically heavy in calcium, suggesting partial evaporative loss of this element (Figs. 10 and 14). However, melts that evaporate calcium should be devoid of magnesium, as it is more volatile and should have been lost before calcium evaporation started (e.g., compare Fig. 2 in Floss et al., 1996; Simon and DePaolo, 2010). If, contrary to expectations, some magnesium was retained in the melt and was incorporated into hibonite upon crystallization, it should be highly mass fractionated. However, all studied CAIs contain magnesium (as a minor element in most hibonites, and as a major element in spinel grains in 1–9–1 and 2–6–1), and mass fractionation in magnesium is minimal or nonexistent in five of these CAIs, including the spinel in 1–9–1 (Figs. 8a and 14a; not assessed in CAIs 2–6–1 and 1–10–3).

Problem (2): In five of the CAIs, mass fractionation effects in oxygen and magnesium are decoupled (Fig. 14a). Experimental studies of CAI melts show that evaporation results in comparable effects in δ^{18}O (equivalent to $\Delta^{18}O_{CCAM}$ if precursor was on the CCAM line) and δ^{25}Mg (Mendybaev et al., 2013). In contrast, most studied CAIs with positive $\Delta^{18}O_{CCAM}$ values (~10‰ to 55‰) lack corresponding enrichments in ^{25}Mg (Fig. 14a). Only one CAI with isotopically heavy oxygen (2–6–6) plots close to the correlation line found by Mendybaev et al., the offset is comparable to the scatter found in other FUN CAIs (Mendybaev et al., 2013, 2017, and references therein).

Problem (3): Most CAIs deviate from the calcium and titanium fractionation trend defined by evaporation experiments using a Ca-,Ti-oxide melt (Zhang et al., 2014; Fig. 10c). While many fall to the right of the trend (i.e., higher F_{Ti} than expected based on their F_{Ca}), three grains show no heavy isotope enrichment in titanium (beyond 3σ) in spite of being among the most fractionated in calcium.

Problem (4): An exercise to constrain the preevaporation compositions for the hibonite-rich CAIs using mass-dependent fractionation effects and mineral chemistry (see Appendix A.1 for details) shows that the inferred precursors of these CAIs are too oxygen-rich (i.e., the inferred relative abundances of O^{2-} are not charge-balanced by cations). To account for the high loss in oxygen, it appears that other elements (e.g., silicon, magnesium) must have evaporated from the precursor melts alongside oxygen. The dataset is therefore not self-consistent.

Volatility considerations associated with problem (1), i.e., presence of magnesium in spite of calcium isotopic fractionation in all studied grains, require that magnesium was (re)introduced into the CAIs after the evaporation event. Ireland et al. (1992) concluded the same for magnesium-bearing HAL-type hibonites with fractionation effects in calcium and titanium. Unless the gas was fractionated from the evaporating melts, the reintroduction of magnesium cannot have occurred by a direct recondensation into the melt following the evaporation event, as calcium should have recondensed before magnesium, which should have

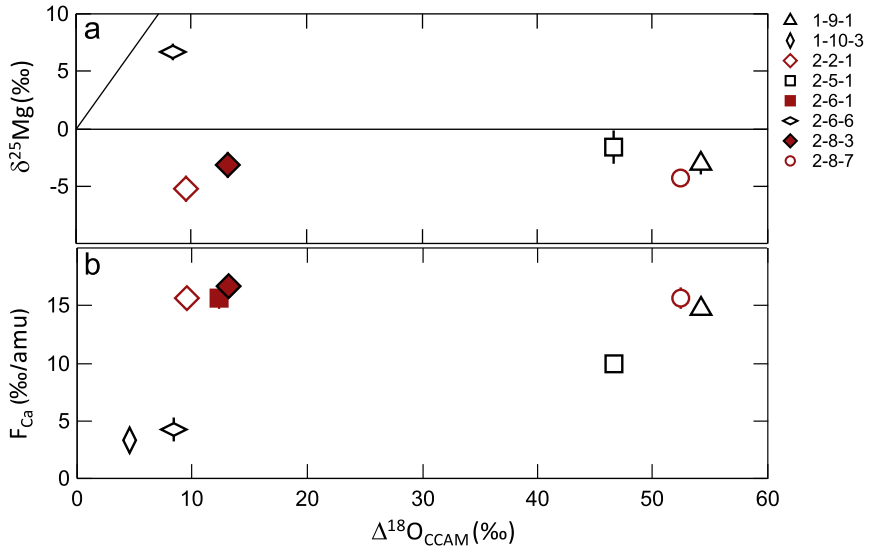

Fig. 14. Comparison of mass fractionation effects between different elements measured in hibonite and grossite. (a) Comparison between fractionation effects in magnesium and oxygen. The black line (slope 1.4) corresponds to the mass-fractionation relationship between oxygen and magnesium derived from melt residues by Mendybaev et al. (2013). (b) Comparison between fractionation effects in calcium and oxygen. Data are single spot analyses or weighted averages if the hibonite grain was analyzed more than once. Uncertainties are 2σ.

erased heavy isotope enrichment in calcium. If true, this implies that mass-dependent fractionation patterns in the studied CAIs cannot be explained by a single high temperature event.

Most fractionated CAIs fall off the steep F_{Ca} vs. F_{Ti} trend defined by Ca-,Ti-oxide evaporation residues (Zhang et al., 2014; problem 3). In particular, many hibonite-rich CAIs, including four CAIs studied here, SHIBs (Kööp et al., 2016b) and four HAL-type hibonites (Ireland et al., 1992), plot to the right of the Zhang et al. (2014) trend (i.e., they have enhanced fractionation in titanium; Fig. 10c). Evaporation experiments of CAI melts with different starting compositions show that a higher relative abundance of an evaporating element can lead to increased evaporation rates and thus higher degrees of mass-dependent fractionation (Mendybaev et al., 2013, 2017). Since the Ca/Ti ratio of the Zhang et al. (2014) melts was close to one, this would suggest that most of the starting compositions of the studied CAIs had Ca/Ti ratios below one. This does not seem likely as the solar Ca/Ti ratio is ~25 (Lodders, 2003) and could suggest that Al-, Ca-,Ti-oxide melts may show a different evaporation behavior than the Ca-,Ti-oxide melts studied by Zhang et al. (2014). Given how many fractionated hibonite-rich CAIs (e.g., HAL-type hibonites from Ireland et al., 1992, SHIBs from Kööp et al., 2016b, four CAIs from this study) as well as evaporation residues of Allende (Floss et al., 1996) plot to the right of Zhang et al. trend, evaporation experiments with more realistic compositions (i.e., with melts that include aluminum and have Ca/Ti ratios closer to solar) may be required to solve this problem.

4.4.2. Solution: Element-specific dilution?

As outlined above, the dataset established here is not self-consistent (Problem 4, Appendix A.1) and the presence of magnesium in seven hibonite-rich CAIs (and its unfractionated character in five of these) is inconsistent with their heavy isotope enrichment in calcium. Similar observations in HAL-type hibonites have been attributed to reintroduction of magnesium after quantitative evaporation, possibly by metamorphism or a reaction with the solar nebula gas (Ireland et al., 1992). Ireland et al. (1992) also consider that surface contamination and 'ion probe knock-on effects' can be responsible for the presence of magnesium in hibonites. For the CAIs studied here, this is unlikely for three reasons. (1) The magnesium contents in three CAIs are so high (i.e., in 1–9–1 Al-Mg spinel was measured in addition to hibonite; 2–2–1 and 2–8–3 have ~1 wt% MgO) that it is unlikely that surface contamination diluted magnesium isotope signatures significantly for these grains. (2) The extraordinarily low MgO content and highly radiogenic Mg isotopic composition of the grossite-rich CAI 2–6–1 indicate that surface contamination is negligible for the studied samples. (3) The hibonite grains studied here show a good correlation between MgO with TiO_2 (as expected for a coupled substitution of Mg^{2+} and Ti^{4+} with two Al^{3+}, Table 1), which suggest that magnesium is present in the hibonite lattice. We further found that for some grains (e.g., 2–2–1, 2–6–6, and 2–8–3; Table 1 and Fig. 6), the abundances of magnesium (and titanium) are higher at grain edges than in the centers. This may support a scenario in which magnesium entered the hibonite lattice by diffusion. Parent body metamorphism is unlikely to be a relevant process as these hibonites were separated from the Murchison CM2 chondrite, a meteorite that shows evidence for aqueous, but not significant thermal processing (e.g., Krot et al., 2014a), leaving reactions with the solar nebula gas at high temperatures as a possible mechanism for introduction of magnesium. Such high temperature events may not only have led to introduction of magnesium into the hibonite lattice, but could have also led to formation of magnesium-rich minerals like spinel in CAIs 1–9–1 and 2–

6–1. Reintroduction of magnesium can also explain the decoupling of fractionation effects in oxygen and magnesium (solution to problem 2).

If magnesium was introduced after the evaporation event, the isotopic signatures of other elements may also have been affected by this event. Among these elements may be titanium, as its abundance is coupled with magnesium in hibonite (coupled substitution; Table 1). An indicator for dilution of mass fractionation effects in titanium could be a small F_{Ti} value in grains with large F_{Ca} values (i.e., analyses plotting in the solid gray region in Fig. 10c). Most prominently, this is observed in platy hibonites 2–2–1 and 2–8–3 (as well as grossite-rich CAI 2–6–1), which are highly fractionated in calcium, but lack any resolvable fractionation in titanium. The hibonites in 2–2–1 and 2–8–3 have the highest abundances of magnesium and titanium (Table 1). If these grains were initially titanium-poor and most of the titanium was reintroduced late alongside magnesium, heavy isotope enrichments in titanium could have been diluted, shifting these grains towards the y-axis in Fig. 10. Low initial titanium abundances in crystallizing fractionated hibonites could have been the result of the lack of a substitution partner (i.e., magnesium). While trivalent titanium could substitute for Al^{3+}, significant abundance of trivalent titanium may be unlikely as the evaporation process itself appears to result in oxidizing conditions and evidence for oxidizing conditions is found in many F(UN) CAIs (Ireland et al., 1992; Floss et al., 1996). Oxidizing conditions are also indicated by the RMNs found in 2–6–6 and 2–5–1, which are highly depleted in Mo and W, elements that are volatile under oxidizing conditions (Fegley and Palme, 1985; Schwander et al., 2015). In summary, it is possible that small F_{Ti} values in some fractionated hibonites with high F_{Ca} values are the result of dilution with isotopically normal titanium that may have entered the hibonite lattice alongside magnesium. While this may explain data falling to the left of the Zhang et al. (2014) trend in Fig. 10c, it does not explain why many grains fall to the right of that trend (i.e., dotted region).

In addition to magnesium and titanium, the oxygen isotopic signatures could have been altered in some hibonites and possibly in grossite in CAI 2–6–1. Candidates for such alteration may be platy hibonites 2–2–1 and 2–8–3, which have F_{Ca} values similar to CAIs 1–9–1 and 2–8–7 (~15‰/amu), but in contrast to 1–9–1 and 2–8–7, their offsets from the CCAM line are small($\Delta^{18}O_{CCAM}$ close to 10‰ vs. >50‰). As noted above, these two grains also contain high amounts of magnesium and titanium, and it may be possible that fractionation in oxygen isotopes was partially erased in these CAIs, perhaps in the same event that diluted isotopic signatures in magnesium and titanium. Since 2–2–1 and 2–8–7 have typical CAI $\Delta^{17}O$ values close to ~–23‰, the most likely reservoir for the exchange is the solar nebula gas, as neither laboratory contamination nor alteration in the parent body are expected to produce this value. Interestingly, the spinel-hibonite platelet 1–9–1, which also contains high amounts of magnesium (in hibonite as well as in the spinel) and may have been affected by reintroduction of titanium, appears to have retained its highly fractionated oxygen isotopic signature (the $\Delta^{18}O_{CCAM}$ values in both spinel and hibonite are the highest among the CAIs studied here). This interpretation would imply that oxygen isotopes remained largely unaffected for some CAIs while magnesium and titanium exchanged (e.g., 1–9–1), while others may have experienced almost complete equilibration in oxygen isotopes (2–2–1 and 2–8–3). A possible solution is that magnesium and titanium exchanged with the solar nebula gas while CAI 1–9–1 was solid, possibly preventing oxygen isotope exchange, while exchange for other CAIs (e.g., 2–2–1 and 2–8–3) may have occurred while these were (re-) melted. However, another interpretation is that 2–2–1 and 2–8–3 formed from higher temperature precursors which had lost less oxygen before calcium evaporation started.

If magnesium and titanium were introduced after the evaporation event, it should also have affected mass-independent signatures. For nucleosynthetic anomalies, introduction of isotopically normal titanium should have reduced ^{50}Ti anomalies (if present) and could be responsible for the observation that anomalies in ^{48}Ca are greater than those in ^{50}Ti (Fig. 11). A postdistillation introduction of isotopically normal titanium (and possibly magnesium) could also explain the variable isotopic compositions Liu et al. (2009) measured in the highly mass-fractionated hibonite aggregate Mur-B1. This CAI is isotopically heavy in titanium and oxygen, which could be indicative of a melt distillation origin. The unexpected internal heterogeneity in titanium isotopes ($\delta^{50}Ti$ range from ~0‰ to ~–46‰) in this CAI could be explained if melt distillation was followed by reintroduction of isotopically normal titanium, as the effect on individual minerals could have been different depending on their proximity to the edge of the inclusion and/or their titanium content. However, we note that Liu et al. (2009) preferred a condensation origin for this CAI due to the lack of cerium depletion and its texture.

Similarly, introduction of magnesium may have affected $\delta^{26}Mg^*$ values and, depending on the timing of the evaporation event, inferred $(^{26}Al/^{27}Al)_0$ ratios. Here, we assume that magnesium entered the hibonite lattice in a one-way reaction, which would probably not result in significant changes in $(^{26}Al/^{27}Al)_0$ as analyses would simply be shifted along possible isochrons. If magnesium evaporation was quantitative (as expected based on measured F_{Ca}), the presence of elevated $\delta^{26}Mg^*$ in some of the CAIs implies that evaporation must have occurred while ^{26}Al was still alive, but we cannot infer when magnesium was added to these CAIs. Evaporation and reintroduction of magnesium can also produce $(^{26}Al/^{27}Al)_0$ of ~0 for ^{26}Al-rich precursors if evaporation and reintroduction events took place after ^{26}Al had fully decayed. However, this scenario is equivalent to a late formation of FUN CAIs after ^{26}Al had decayed and has the same problems as outlined in Section 1. We therefore prefer the interpretation in which the isotopically anomalous CAIs with $(^{26}Al/^{27}Al)_0 \sim 0$ formed early in a ^{26}Al-poor reservoir.

Among the studied elements, calcium may be the best recorder of primary nucleosynthetic and mass-fractionation effects in hibonite. This is indicated foremost by 2–2–1 and 2–8–3, which preserve large fractionation effects in calcium, but appear to have experienced the most extensive reintroduction of magnesium, and possibly dilu-

tion of isotopic effects in oxygen and titanium (Figs. 7, 8 and 10). In addition, calcium preserves nucleosynthetic anomalies for all ^{26}Al-poor fractionated hibonites (1–9–1, 2–5–1, 2–6–6). In contrast to elements like magnesium and titanium, exchange or reintroduction of calcium may be inhibited by mineral chemistry (Murchison hibonites show no significant substitution for calcium, e.g., Kööp et al., 2016a,b).

5. CONCLUSIONS

1. Mass-fractionated hibonite- and grossite-rich CAIs span a range of inferred initial ^{26}Al/^{27}Al ratios from approximately zero to canonical. They show a mutual exclusivity relationship between inferred incorporation of live ^{26}Al and the presence of resolvable anomalies in ^{48}Ca and ^{50}Ti, just as has been observed in non-F(UN) hibonite-rich CAIs (Kööp et al., 2016a,b). This suggests that these CAIs sampled two distinct reservoirs: an ^{26}Al-poor, isotopically anomalous reservoir and a well-mixed reservoir that contained live ^{26}Al. If these reservoirs formed because the solar nebula evolved from an initially isotopically heterogeneous towards a more homogeneous stage over time, the data can be interpreted such that fractionated CAIs formed over an extended time period and sampled the following stages in the isotopic evolution of the solar nebula: (1) an ^{26}Al-poor nebula with large positive and negative anomalies in ^{48}Ca and ^{50}Ti; (2) a period of ^{26}Al-admixture, during which anomalies in ^{48}Ca and ^{50}Ti had been largely diluted; and (3) a nebula with an approximately canonical level of ^{26}Al in the CAI formation region. This interpretation suggests that conditions favorable for forming these highly fractionated, refractory objects existed for an extended period of time. Since both fractionated and unfractionated CAIs seem to have recorded the ^{26}Al-poor anomalous nebula as well as the ^{26}Al-rich nebula, it appears that CAIs formed over an extended time via distinct processes or under distinct conditions, either simultaneously at different solar radii, or alternating in the hot regions close to the Sun.
2. The hibonite-rich fractionated CAIs studied here show a link between inferred initial ^{26}Al/^{27}Al ratios and Δ^{17}O values. The CAIs with low inferred initial ^{26}Al/^{27}Al ratios show a resolved range of Δ^{17}O values, while CAIs with possible incorporation of ^{26}Al (^{26}Al/^{27}Al between $(0.348 \pm 0.058) \times 10^{-5}$ and canonical) have Δ^{17}O values close to the common CAI value of ~–23‰ (Makide et al., 2009; Bullock et al., 2012; Kööp et al., 2016b; Ushikubo et al., 2017). This could suggest that the oxygen isotopic composition of the CAI formation region was variable before fresh ^{26}Al arrived, and had been (temporarily) stabilized at a Δ^{17}O value of ~–23‰ while ^{26}Al was being admixed. The mass-fractionated hibonite-rich CAIs studied by Liu et al. (2009) appear to be consistent with this relationship: the ^{26}Al-poor CAI Mur-B1 is less ^{16}O-rich (Δ^{17}O ~ –14‰) than the fractionated CAI with a positive ^{26}Al/^{27}Al (CH A5; listed Δ^{17}O values of spot analyses are ~–22‰, Liu et al., 2009). In contrast, fractionated CAI Kz1-2 is apparently inconsistent with this relationship, as it has an elevated Δ^{17}O value (~–17‰) and approximately canonical abundance of ^{26}Al (Ushikubo et al., 2007). However, in contrast to the CAIs studied here, the oxide phases in Kz1-2 are FeO-rich, which indicates that it experienced different alteration processes than the CAIs studied here.
3. The grossite-rich CAI, which has an inferred ^{26}Al/^{27}Al ratio close to canonical, is slightly depleted in ^{16}O (Δ^{17}O ~ –17‰). This CAI could have formed from slightly ^{16}O-depleted material, recorded variations in the oxygen isotopic composition of the CAI formation region, or exchanged with a ^{16}O-poor reservoir after formation. The latter could indicate that grossite may be more susceptible to exchange than hibonite.
4. This study confirms that mass-dependent fractionation effects can be observed in refractory hibonite- and grossite-rich CAIs that belong to different populations based on their nucleosynthetic and radiogenic isotope characteristics. Similar to previous studies, we attribute heavy isotope enrichment to melt evaporation in the solar nebula. Heavy isotope enrichment was observed in all studied elements, but never simultaneously in all elements in the same CAI.
5. The presence of unfractionated or isotopically light magnesium in hibonites with heavy isotope enrichment in calcium suggests that magnesium was (re-) introduced into the CAIs after the evaporation event (also see Ireland et al., 1992). The correlation between magnesium and titanium contents in these hibonites may suggest that for some of these CAIs, titanium could have (re-)entered the hibonite lattice alongside magnesium.
6. Most hibonite data indicate preferential evaporative loss of titanium relative to calcium (relative to the calcium and titanium evaporation trend established by Zhang et al., 2014). This result may suggest that calcium-, titanium-, and aluminum-rich oxide melts show a different evaporation behavior than the calcium- and titanium-rich oxide melts studied by Zhang et al. (2014).
7. All eight studied CAIs preserve mass-dependent fractionation in calcium isotopes. The largest nucleosynthetic anomalies are also found in this element (in ^{48}Ca). This could indicate that calcium is more robust to isotopic dilution, possibly because it is fixed by hibonite stoichiometry (all Murchison hibonites have ~8.5 wt % CaO, corresponding to one Ca atom per formula unit, while magnesium and titanium contents are variable). If postevaporation processes affected the titanium and/or oxygen isotopic compositions of the studied hibonite-rich CAIs, the variability found in mass-dependent signatures suggests that these processes occurred in distinct reservoirs and/or under distinct conditions for almost every CAI. However, it cannot be excluded that the calcium, titanium, and oxygen isotopic signatures are primary and reflect the evaporation process. In this case, the lack of trends is likely the result of different pre-evaporation compositions.

ACKNOWLEDGEMENTS

We thank Ian Steele for his help with EPMA analyses and Frank Richter for helpful discussions. We thank guest editor C. Floss for editorial handling. Reviews from G. MacPherson and two anonymous reviewers helped improve this paper. This work is part of a doctoral dissertation by L. Kööp and was supported through a NASA Earth and Space Science Fellowship. We acknowledge funding from the NASA Cosmochemistry Program (grant NNX09AG39G to A. M. Davis, grants NNX11AG62G and NNX14AG29G to N. T. Kita), NASA Laboratory Analysis of Returned Samples Program (grant NNX15AF78G to A. M. Davis, grant NNX13AD15G to N. T. Kita) and NASA Emerging Worlds Program (grant NNX15AH38G to A. N. Krot). WiscSIMS is partly supported by NSF (EAR03-19230, EAR10-53466, EAR13-55590). P. R. Heck acknowledges funding from the Tawani Foundation. C. Park was partly supported by KOPRI grant (PM16030). This paper is dedicated to the memory of Ernst Zinner.

APPENDIX A

A.1. Balancing and attempting to constrain the precursor compositions

The variability of mass fractionation effects observed in the eight CAIs could be a result of formation from precursor melts with different starting compositions (note that this is not a solution to problem 1). For example, with an F_{Ca} of ~15‰/amu and a $\Delta^{18}O_{CCAM}$ of ~10‰, CAI 2-2-1 may have formed from a more refractory precursor than CAI 2-8-7, which has a similar F_{Ca}, but a $\Delta^{18}O_{CCAM}$ of ~55‰, suggesting that a larger fraction of oxygen was lost, possibly alongside less refractory elements like magnesium or silicon.

Using the mass-fractionation data and experimentally established fractionation factors (here, values from Mendybaev et al., 2013, are used for oxygen and from Zhang et al., 2014, for calcium and titanium), one can attempt to constrain the pre-evaporation compositions of these CAIs. The problem for this calculation is that the loss of less volatile elements like magnesium and silicon, which might have been present in some of the precursor melts, cannot be estimated because of the lack of heavy isotope enrichment in magnesium preserved in all but one of the hibonite-rich CAIs and the lack of data for silicon. Because of this, magnesium and silicon loss are not considered in the calculations. It further needs to be assumed that the refractory element aluminum did not evaporate, as its loss cannot be assessed (aluminum has only one stable isotope). Finally, we assume that the EPMA analyses reported in Table 1 correspond to the bulk composition of the evaporation residues (i.e., small perovskite inclusions are not considered, and it is assumed that the grains were not liberated from a larger assemblage of different bulk chemistry). Even for spinel-hibonite platelet, using the hibonite chemistry for the bulk composition is a reasonable assumption for this exercise, because aluminum and magnesium are not considered for the balancing. This exercise suggests losses of ~10–90% for titanium, ~30–80% for calcium, and 20–90% for oxygen (Table A.1). Since the relative abundances of oxygen are significantly higher than those of calcium and titanium, the resulting pre-evaporation compositions are extremely oxygen-enriched and not charge-balanced. This suggests that evaporation of calcium and titanium alone cannot account for the loss in oxygen in the seven CAIs and that other elements must have evaporated from the melts to account for the loss in oxygen. This could indicate that all CAIs formed from lower temperature precursors that contained elements like silicon and magnesium, which evaporated alongside oxygen prior to the evaporation of refractory elements. However, some CAI melts may also have lost aluminum, which could make a large difference here as it is the most abundant cation in hibonite. Furthermore, the assumption that the studied CAIs are the sole residues of the evaporation process is questionable, which may have affected the results of this calculation.

In summary, based on the available data, it appears that the mass-fractionation effects in oxygen, calcium, and titanium are not self-consistent for the hibonite analyses and that different precursor compositions alone cannot explain the mass-fractionation data established here.

APPENDIX B. SUPPLEMENTARY MATERIAL

Supplementary data associated with this article can be found, in the online version, at http://dx.doi.org/10.1016/j.gca.2017.04.029.

REFERENCES

Amari S., Lewis R. S. and Anders E. (1994) Interstellar grains in meteorites. I – Isolation of SiC, graphite, and diamond; size distributions of SiC and graphite. *Geochim. Cosmochim. Acta* **58**, 459–470.

Birck J.-L. (2004) An overview of isotopic anomalies in extraterrestrial materials and their nucleosynthetic heritage. *Rev. Mineral. Geochem.* **55**, 25–64.

Bullock E. S., MacPherson G. J., Nagashima K., Krot A. N., Petaev M. I., Jacobsen S. B. and Ulyanov A. A. (2012) Forsterite-bearing type B refractory inclusions from CV3 chondrites: from aggregates to volatilized melt droplets. *Meteorit. Planet. Sci.* **47**, 2128–2147.

Clayton R. N., Hinton R. W. and Davis A. M. (1988) Isotopic variations in the rock-forming elements in meteorites. *Phil. Trans. R. Soc. Lond.* **A325**, 483–501.

Dauphas N., Chen J. H., Zhang J., Papanastassiou D. A., Davis A. M. and Travaglio C. (2014) Calcium-48 isotopic anomalies in bulk chondrites and achondrites: evidence for a uniform isotopic reservoir in the inner protoplanetary disk. *Earth Planet. Sci. Lett.* **407**, 96–108.

Dauphas N. and Schauble E. A. (2016) Mass fractionation laws, mass-independent effects, and isotopic anomalies. *Annu. Rev. Earth Planet. Sci.* **44**, 709–783.

Davis A. M., Richter F. M., Mendybaev R. A., Janney P. E., Wadhwa M. and McKeegan K. D. (2005) Isotopic mass fractionation laws and the initial solar system $^{26}Al/^{27}Al$ ratio. *Lunar Planet. Sci.* **36**, 2334.

Davis A. M., Richter F. M., Mendybaev R. A., Janney P. E., Wadhwa M. and McKeegan K. D. (2015) Isotopic mass fractionation laws for magnesium and their effects on ^{26}Al-^{26}Mg systematics in solar system materials. *Geochim. Cosmochim. Acta* **158**, 245–261.

Esat T. M., Lee T., Papanastassiou D. A. and Wasserburg G. J. (1978) Search for ^{26}Al effects in the Allende FUN inclusion C1. *Geophys. Res. Lett.* **5**, 807–810.

Fahey A. J., Goswami J. N., McKeegan K. D. and Zinner E. (1987) ^{26}Al, ^{244}Pu, ^{50}Ti, REE, and trace element abundances in hibonite grains from CM and CV meteorites. *Geochim. Cosmochim. Acta* **51**, 329–350.

Fegley, Jr., B. and Palme H. (1985) Evidence for oxidizing conditions in the solar nebula from Mo and W depletions in refractory inclusions in carbonaceous chondrites. *Earth Planet. Sci. Lett.* **72**, 311–326.

Floss C., El Goresy A., Zinner E., Kransel G., Rammensee W. and Palme H. (1996) Elemental and isotopic fractionations produced through evaporation of the Allende CV chondrite: implications for the origin of HAL-type hibonite inclusions. *Geochim. Cosmochim. Acta* **60**, 1975–1997.

Holst J. C., Olsen M. B., Paton C., Nagashima K., Schiller M., Wielandt D., Larsen K. K., Connelly J. N., Jørgensen J. K., Krot A. N., Nordlund Å. and Bizzarro M. (2013) ^{182}Hf-^{182}W age dating of a ^{26}Al-poor inclusion and implications for the origin of short-lived radioisotopes in the early Solar System. *Proc. Natl. Acad. Sci. U.S.A.* **110**, 8819–8823.

Ireland T. R. (1988) Correlated morphological, chemical, and isotopic characteristics of hibonites from the Murchison carbonaceous chondrite. *Geochim. Cosmochim. Acta* **52**, 2827–2839.

Ireland T. R. (1990) Presolar isotopic and chemical signatures in hibonite-bearing refractory inclusions from the Murchison carbonaceous chondrite. *Geochim. Cosmochim. Acta* **54**, 3219–3237.

Ireland T. R., Zinner E. K., Fahey A. J. and Esat T. M. (1992) Evidence for distillation in the formation of HAL and related hibonite inclusions. *Geochim. Cosmochim. Acta* **56**, 2503–2520.

Jacobsen B., Yin Q., Moynier F., Amelin Y., Krot A. N., Nagashima K., Hutcheon I. D. and Palme H. (2008) ^{26}Al-^{26}Mg and ^{207}Pb-^{206}Pb systematics of Allende CAIs: Canonical solar initial ^{26}Al/^{27}Al ratio reinstated. *Earth Planet. Sci. Lett.* **272**, 353–364.

Kawasaki N., Itoh S., Sakamoto N. and Yurimoto H. (2017) Chronological study of oxygen isotope composition for the solar protoplanetary disk recorded in a fluffy Type A CAI from Vigarano. *Geochim. Cosmochim. Acta* **201**, 83–102.

Kita N. T., Nagahara H., Tachibana S., Tomomura S., Spicuzza M. J., Fournelle J. H. and Valley J. W. (2010) High precision SIMS oxygen three isotope study of chondrules in LL3 chondrites: role of ambient gas during chondrule formation. *Geochim. Cosmochim. Acta* **74**, 6610–6635.

Kita N. T., Ushikubo T., Fu B. and Valley J. W. (2009) High precision SIMS oxygen isotope analysis and the effect of sample topography. *Chem. Geol.* **264**, 43–57.

Kita N. T., Ushikubo T., Knight K. B., Mendybaev R. A., Davis A. M., Richter F. M. and Fournelle J. H. (2012) Internal ^{26}Al-^{26}Mg isotope systematics of a Type B CAI: remelting of refractory precursor solids. *Geochim. Cosmochim. Acta* **86**, 37–51.

Kööp L., Davis A. M., Nakashima D., Park C., Krot A. N., Nagashima K., Tenner T. J., Heck P. R. and Kita N. T. (2016a) A link between oxygen, calcium and titanium isotopes in ^{26}Al-poor hibonite-rich CAIs from Murchison and implications for the heterogeneity of dust reservoirs in the solar nebula. *Geochim. Cosmochim. Acta* **189**, 70–95.

Kööp L., Nakashima D., Heck P. R., Kita N. T., Tenner T. J., Krot A. N., Nagashima K., Park C. and Davis A. M. (2016b) New constraints on the relationship between ^{26}Al and oxygen, calcium, and titanium isotopic variation in the early Solar System from a multielement isotopic study of spinel-hibonite inclusions. *Geochim. Cosmochim. Acta* **184**, 151–174.

Krot A. N., Nagashima K., Ciesla F. J., Meyer B. S., Hutcheon I. D., Davis A. M., Huss G. R. and Scott E. R. D. (2010) Oxygen isotopic composition of the Sun and mean oxygen isotopic composition of the protosolar silicate dust: evidence from refractory inclusions. *Astrophys. J.* **713**, 1159–1166.

Krot A.N., Keil K., Scott E.R.D., Goodrich C.A., and Weisberg M.K. (2014a). Classification of meteorites and their genetic relationships. In Meteorites and Cosmochemical Processes (Ed. A. M. Davis), Vol. 1 Treatise on Geochemistry, 2nd Ed. (Exec. Eds. H. D. Holland and K. K. Turekian), Elsevier, Oxford, pp. 1–63.

Krot A. N., Nagashima K., Wasserburg G. J., Huss G. R., Papanastassiou D., Davis A. M., Hutcheon I. D. and Bizzarro M. (2014b) Calcium-aluminum-rich inclusions with fractionation and unknown nuclear effects (FUN CAIs): I. Mineralogy, petrology, and oxygen isotopic compositions. *Geochim. Cosmochim. Acta* **145**, 206–247.

Lee T., Russell W. A. and Wasserburg G. J. (1979) Calcium isotopic anomalies and the lack of aluminum-26 in an unusual Allende inclusion. *Astrophys. J.* **228**, L93–L98.

Liu M.-C., Chaussidon M., Göpel C. and Lee T. (2012) A heterogeneous solar nebula as sampled by CM hibonite grains. *Earth Planet. Sci. Lett.* **327**, 75–83.

Liu M.-C., McKeegan K. D., Goswami J. N., Marhas K. K., Sahijpal S., Ireland T. R. and Davis A. M. (2009) Isotopic records in CM hibonites: implications for timescales of mixing of isotope reservoirs in the solar nebula. *Geochim. Cosmochim. Acta* **73**, 5051–5079.

Lodders K. (2003) Solar system abundances and condensation temperatures of the elements. *Astrophys. J.* **591**, 1220–1247.

Loss R. D., Lugmair G. W., Davis A. M. and MacPherson G. J. (1994) Isotopically distinct reservoirs in the solar nebula: isotope anomalies in Vigarano meteorite inclusions. *Astrophys. J.* **436**, L193–L196.

MacPherson G. J. (2014). Calcium–aluminum-rich inclusions in chondritic meteorites. In Meteorites and Cosmochemical Processes (Ed. A. M. Davis), Vol. 1 Treatise on Geochemistry, 2nd Ed. (Exec. Eds. H. D. Holland and K. K. Turekian), Elsevier, Oxford, pp. 139–179.

Makide K., Nagashima K., Krot A. N., Huss G. R., Hutcheon I. D. and Bischoff A. (2009) Oxygen- and magnesium-isotope compositions of calcium-aluminum-rich inclusions from CR2 carbonaceous chondrites. *Geochim. Cosmochim. Acta* **73**, 5018–5050.

Makide K., Nagashima K., Krot A. N., Huss G. R., Hutcheon I. D., Hellebrand E. and Petaev M. I. (2013) Heterogeneous distribution of 26Al at the birth of the Solar System: Evidence from corundum-bearing refractory inclusions in carbonaceous chondrites. *Geochim. Cosmochim. Acta* **110**, 190–215.

McKeegan K. D., Kallio A. P. A., Heber V. S., Jarzebinski G., Mao P. H., Coath C. D., Kunihiro T., Wiens R. C., Nordholt J. E., Moses R. W., Reisenfeld D. B., Jurewicz A. J. G. and Burnett D. S. (2011) The oxygen isotopic composition of the Sun inferred from captured solar wind. *Science* **332**, 1528–1532.

Mendybaev R. A., Richter F. M., Georg R. B., Janney P. E., Spicuzza M. J., Davis A. M. and Valley J. W. (2013) Experimental evaporation of Mg- and Si-rich melts: implications for the origin and evolution of FUN CAIs. *Geochim. Cosmochim. Acta* **123**, 368–384.

Mendybaev R. A., Williams C. D., Spicuzza M. J., Richter F. M., Valley J. W., Fedkin A. V. and Wadhwa M. (2017) Thermal and chemical evolution in the early Solar System as recorded by FUN CAIs: Part II – laboratory evaporation of potential CMS-1 precursor material. *Geochim. Cosmochim. Acta* **201**, 49–64.

Niederer F. R. and Papanastassiou D. A. (1984) Ca isotopes in refractory inclusions. *Geochim. Cosmochim. Acta* **48**, 1279–1293.

Niederer F. R., Papanastassiou D. A. and Wasserburg G. J. (1981) The isotopic composition of titanium in the Allende and Leoville meteorites. *Geochim. Cosmochim. Acta* **45**, 1017–1031.

Ogliore R. C., Huss G. R. and Nagashima K. (2011) Ratio estimation in SIMS analysis. *Nucl. Instrum. Meth. Phys. Res. B* **269**, 1910–1918.

Palme H., Borisov A. and Wulf A. V. (1998) Experimental determination of the oxidation sequence of refractory metals. *Lunar Planet. Sci.* **29**, 1611.

Papanastassiou D. A. and Brigham C. A. (1987) FUN isotopic anomalies: reincarnation in purple refractory inclusions (abstract). *Lunar Planet. Sci.* **18**, 756–757.

Papanastassiou D. A. and Brigham C. A. (1988) Correlated, large isotope effects in purple, spinel-rich inclusions (abstract). *Lunar Planet. Sci.* **19**, 899–900.

Park C., Nagashima K., Krot A. N., Huss G. R., Davis A. M. and Bizzarro M. (2017) Calcium-aluminum-rich inclusions with fractionation and unidentified nuclear effects (FUN CAIs): II. Heterogeneities of magnesium isotopes and ^{26}Al in the early Solar System inferred from *in situ* high-precision magnesium-isotope measurements. *Geochim. Cosmochim. Acta* **201**, 6–24.

Park C., Nagashima K., Wasserburg G. J., Papanastassiou D. A., Hutcheon I. D., Davis A. M., Huss G. R., Bizzarro M. and Krot A. N. (2014) Calcium and titanium isotopic compositions of FUN CAIs: implications for their origin. *Lunar Planet. Sci.* **45**, 2656.

Rout S. S., Bischoff A., Nagashima K., Krot A. N., Huss G. R. and Keil K. (2009) Oxygen- and magnesium-isotope compositions of calcium–aluminum-rich inclusions from Rumuruti (R) chondrites. *Geochim. Cosmochim. Acta* **73**, 4264–4287.

Sahijpal S. and Goswami J. N. (1998) Refractory phases in primitive meteorites devoid of ^{26}Al and ^{41}Ca: representative samples of first Solar System solids? *Astrophys. J. Lett.* **509**, L137–L140.

Sahijpal S., Goswami J. N. and Davis A. M. (2000) K, Mg, Ti and Ca isotopic compositions and refractory trace element abundances in hibonites from CM and CV meteorites: implications for early solar system processes. *Geochim. Cosmochim. Acta* **64**, 1989–2005.

Schwander D., Kööp L., Berg T., Schönhense G., Heck P. R., Davis A. M. and Ott U. (2015) Formation of refractory metal nuggets and their link to the history of CAIs. *Geochim. Cosmochim. Acta* **168**, 70–87.

Simon J. I. and DePaolo D. J. (2010) Stable calcium isotopic composition of meteorites and rocky planets. *Earth Planet. Sci. Lett.* **289**, 457–466.

Trinquier A., Elliott T., Ulfbeck D., Coath C., Krot A. N. and Bizzarro M. (2009) Origin of nucleosynthetic isotope heterogeneity in the solar protoplanetary disk. *Science* **324**, 374–376.

Ushikubo T., Hiyagon H. and Sugiura N. (2007) A FUN-like inclusion with a large ^{26}Mg-excess. *Earth Planet. Sci. Lett.* **254**, 115–126.

Ushikubo T., Nakashima D., Kimura M., Tenner T. J. and Kita N. T. (2013) Contemporaneous formation of chondrules in distinct oxygen isotope reservoirs. *Geochim. Cosmochim. Acta* **109**, 280–295.

Ushikubo T., Tenner T. J., Hiyagon H. and Kita N. T. (2017) A long duration of the ^{16}O-rich reservoir in the solar nebula, as recorded in fine-grained refractory inclusions from the least metamorphosed carbonaceous chondrites. *Geochim. Cosmochim. Acta* **201**, 103–122.

Williams C. D., Ushikubo T., Bullock E. S., Janney P. E., Hines R. R., Kita N. T., Hervig R. L., MacPherson G. J., Mendybaev R. A., Richter F. M. and Wadhwa M. (2017) Thermal and chemical evolution in the early solar system as recorded by FUN CAIs: Part I – petrology, mineral chemistry, and isotopic composition of Allende FUN CAI CMS-1. *Geochim. Cosmochim. Acta* **201**, 25–48.

Wimpenny J. B., Yin Q.-Z., Zipfel J., MacPherson G. and Ebel D. S. (2014) Renewed search for FUN based on Al-Mg systematics in CAIs with LA-MC-ICP-MS. *Lunar Planet. Sci.* **45**, 2235.

Wood J. A. (1998) Meteoritic evidence for the infall of large interstellar dust aggregates during the formation of the Solar System. *Astrophys. J.* **503**, L101–L104.

Zhang J., Huang S., Davis A. M., Dauphas N., Hashimoto A. and Jacobsen S. B. (2014) Calcium and titanium isotopic fractionations during evaporation. *Geochim. Cosmochim. Acta* **140**, 365–380.

Zinner E. K., Fahey A. J., Goswami J. N., Ireland T. R. and McKeegan K. D. (1986) Large ^{48}Ca anomalies are associated with ^{50}Ti anomalies in Murchison and Murray hibonites. *Astrophys. J. Lett.* **311**, L103–L107.

Zinner E. K., Fahey A. J., McKeegan K. D. and Goswami J. N. (1987) Isotopic structures in Murchison hibonites: O, Ca, and Ti. *Meteoritics* **22**, 542–543.

Associate editor: Anders Meibom